Multiferroic Materials for Next-Generation Power Amplifiers

Final Report
(Contract No. AFRL FA8650-09-1-7970)

J. Stevenson Kenney (PI), W. Alan Doolittle (co-PI),

John Papapolymerou(co-PI),

Georgia Institute of Technology

School of Electrical and Computer Engineering

777 Atlantic Dr. NW

Atlanta, GA 30332-0250

Table of Contents

1. Executive Summary

The purpose of this seedling research project was to investigate the feasibility of using multiferroic materials for advanced RF applications. The project was divided into three parallel tasks:

1) Materials growth
2) Device design
3) Circuit design

The materials growth effort was specifically aimed at epitaxial quality Terfenol-D, an alloy of Terbium, Dysprosium, and Iron ($Tb_xDy_{1-x}Fe_{2-y}$) that exhibits large magnetostriction at room temperature and relatively small applied magnetic fields. The use of a piezoelectric substrate was proposed to provide the mechanical coupling necessary to achieve electric-field tunable materials. An initial approach using one MBE chamber was explored. However, mechanical issues prevented this approach from yielding any usable materials. A secondary approach was attempted using separate MBE chambers and vacuum-locked wafer transport. Some results were obtained using this technique. However, oxidation of the metal layers, particularly Tb, prevented any successful alloyed-layer growth of Terfenol-D.

The device design task consisted of electromagnetic simulation of transmission line structures, specifically coplanar waveguide (CPW), using Terfenol-D layers on Lithium Niobate ($LiNbO_3$) substrates. Simulations of phase velocity change were conducted to assess the extent to which the magnetic properties (permeability) of Terfenol-D would change the phase velocity. Of course, the phase velocity change was also due to the change in permittivity of the piezoelectric substrate. Simulations indicated approximately a 1.4:1 change in phase velocity could result from the shifts in permittivity and permeability due to an applied bias voltage. Such phase velocity changes could result in usuable devices for various tunable RF applications.

The circuit design aspect of this project consisted entirely of a study of parametric amplifiers (paramps). Such amplifiers result from a change in reactive impedance (*i.e.* associated with a phase velocity change) due to applied RF voltages. In this manner, high-efficieciency, and potentially wideband RF power amplifiers could be achieved. Because this task was executed in parallel with the materials growth and device design, no circuit designs using multiferroic materials was possible. Instead, conventional semiconductor varactor devices were used to assess the feasibility of RF power paramps. Extensive circuit modelling was performed, and prototype circuits were constructed. Some successes were achieved in the development of wideband amplifiers based on double-balanced mixer circuit topologies. In addition, efficiencies approaching 50% were achieve for narrow band parametric amplifiers.

In conclusion, it is clear that significantly more research must be performed on multiferroic materials growth in order to achieve any successes at the device or circuit level. If sufficient improvement in materials quality is obtained, the device and circuit simulations and prototypes indicate some feasibility of the approach of using multiferroic materials for advanced RF applications.

2. Multiferroic Materials Development

A. History of Magnetostrictive Materials

Magnetostrictive materials undergo a change in shape, at roughly constant volume, due to a change in magnetization. Conversely, these materials also exhibit the inverse effect, known as the Villari effect, where in a change in shape induces a change in magnetization. Most ferromagnetic materials are magnetostrictive and result in the audible transformer "humming" commonly heard. For simple ferromagnetic materials such as iron, and cobalt, the changes in dimensions are small due to the Joule magnetostriction mechanism, typically on the order of 10 parts per million. This Joule magnetostriction has been known for more than ~120 years. However, recent discoveries of iron/gallium alloys, termed Galfenol, show magnetostriction on the order of 400 ppm, ~20-40X greater than simple Joule type magnetostriction. While the mechanism for which these materials operate is still controversial, many now feel that these materials operate based on an extreme version of the Joule mechanism.

During the 1960's, a form of gigantic magnetostriction was discovered by Navy researchers lead by A. E. Clarke. These magnetostrictive materials exhibit 1000's of ppm magnetostriction and have only been found in rare earth alloys. The undisputed king of these giant magnetostriction alloys is Terfenol-D, an alloy of Terbium, Dysprosium, and Iron ($Tb_xDy_{1-x}Fe_{2-y}$) that exhibits large magnetostriction at room temperature and relatively small applied magnetic fields. Other combinations of rare earth alloys had application restricting problems centered on the large magnetostriction only appearing at very large magnetic fields, or cryogenic temperatures. Terfenol-D is somewhat unique in that its curie temperature is above room temperature (>350 °C) making it viable for real world applications. By carefully controlling the ratio of Terbium and Dysprosium the "effective anisotropy" can be controlled to ~zero at room temperature making it sensitive to small applied magnetic fields common in power RF applications as proposed herein.

It should be noted that materials do exist that have even higher magnetostriction than Terfonol-D. Most notably the NiMnGa ferromagnetic shape change alloys can exhibit several percent magnetostriction. However, for the purposes proposed herein, the fundamental mechanism for this enormous magnetostriction make the inverse effect, the Villari effect, smaller than in Terfenol-D and thus not relevant to the proposed devices and circuits. Specifically, in these materials, a crystalline twin boundary is "unzipped" under application of a magnetic field causing a large lattice distortion. Unfortunately, this is not driven by strain effects and thus, the Villari effect is smaller in these materials. Much discussion is given in the literature to the magnetostriction effect, largely because most previous applications were in actuators or sensors. However, the primary mode of operation in the devices and circuits proposed herein is from the Villari effect making materials with large Villari coefficients of more interest. Terfenol-D is the champion material for this application.

There are two categories of magneto-electric materials to be considered:

Ceramic composites, and epitaxial materials. The former have been shown to exhibit considerable magnetostrictive behavior, as well as the inverse effect when bonded to a piezoelectric layer [Nan, *et al.*]. However, due to mechanical losses and other mechanisms, dynamic ferroelectric responses are limited to below 1 MHz for polymer-based composites, thus rendering them useless for microwave application. Ceramic composites have been shown to work at microwave frequencies, albeit with very limited tunability. For these reasons, we will restrict our attention to epitaxial multiferroic materials that do not exhibit such shortcomings.

B. Magnetostrictive Materials Behavior and Impact on Devices and Circuits

Gigantic magnetostrictive materials like Terfenol-D possess magnetic domains that can be realigned with application of an external applied magnetic field. The realignment results is a shape distortion which changes the dimensions of the material along a given direction- magnetostriction. Conversely, if strain is applied, either by mechanical loading, epitaxial lattice mismatch or applied through a piezoelectric transducer, the domains can also re-align changing in turn, the magnetization– the Villari effect. The direction and magnitude of the magnetic field depends on the crystalline orientation and the applied strain. Thus, all properties must be considered as tensor quantities, complicating device design and optimization. Bulk materials have shown a clear advantage of "preloading" where in the material is mechanically clamped so as to exhibit increased magnetostriction. Figure 2.1 shows the strong effect of strain

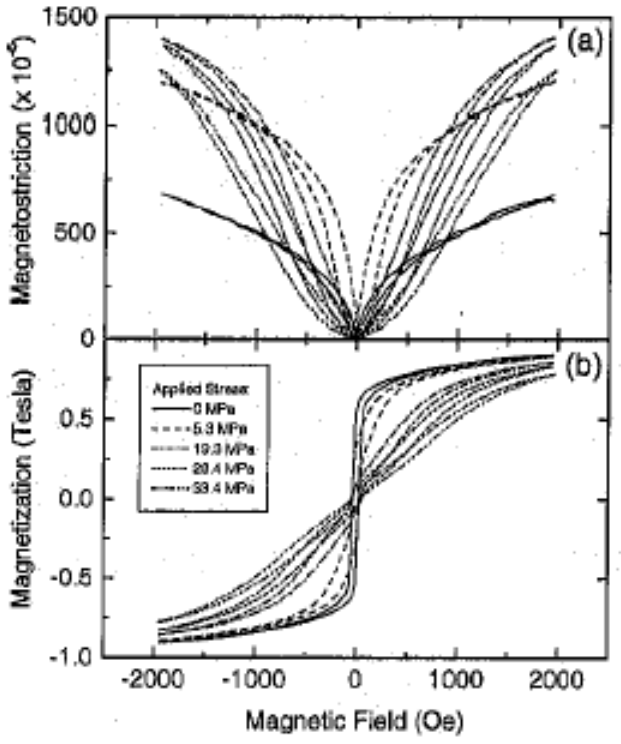

Fig. 2.1: Magnetization vs. magnetic field and strain for bulk Terfenol-D after [M. Wun-Fogle, *et al.*] Note the large strain induced changes in permeability and the large saturation magnetism which is approximately constant with strain.

on the magnetostriction and more importantly for this application the permeability (slope of bottom curve in Figure 5). However, the epitaxial methods can achieve this "preload" by more flexible means including choice of substrate and thus lattice match, or even by growth temperature so as to achieve differing strain from differences in thermal expansion between film and substrate upon cooling to room temperature. Thus, not only can epitaxial Terfenol-D materials produce the highest quality films with minimal RF dispersion, but the process can also tune the strain in order to reach an optimal Villari coefficient.

C. Important Properties of Terfenol-D

Terfenol-D is brittle metal with hexagonal lattice constants, a≈5.189 and c≈12.821 Å (variations occur as the composition of Dy and Tb change – even slightly). These lattice constant values will be of paramount importance for the proposed implementations as we will demonstrate that Terfenol-D may be grown in single crystalline thin film form on a commonly available piezoelectric material which itself has one of the highest mechanical coupling coefficients. Another key feature critical for our proposed application is the very large saturation magnetization, ~1 Tesla, at room temperature and the strain independence of this saturation magnetism (see figure 1 for example). For applications where RF power is considered or where devices will operate in resonance where stored energy density is high, saturation magnetism acts as an upper limit to the electromagnetic power capabilities of the device and thus should be as high as possible. If RF power causes internal fields to exceed the saturation limit, the device begins to act as a saturable absorber or effectively as a limiter. While this may be desirable for other RF applications, it is an undesirable feature in the present device proposal. Additionally, all previous applications where large magnetostriction coefficients were obtained (Vieland et al for example) required highly deformable composite materials which are too soft (acoustically) for high frequency operation. Terfenol-D is a rigid material with an elastic modulus ranging in the 10-80 Gigapascal range, affording it the ability to be used at high frequencies where acoustic losses must be minimized. This last point comes about with some complication. The modulus is dependent on the initial strain state (i.e. is non-linear) and the applied magnetic field. While this might be viewed as a negative for a linear circuit, it enhances the non-linearity at the core of operation in the parametric amplifier, possibly amplifying the parametric effect. For large fields (high RF Power) the modulus will continuously change as the magnetic field increases during the RF cycle. Furthermore, when grown on a piezoelectric material which is being strained by the RF electric field, the modulus will also be strained. The complexity of this situation results in the possibility of multiple resonances that can be exploited in the parametric amplifier design.

Georgia Tech proposed to advance the state to the art in multiferroic thin films by epitaxially growing Terfenol-D on a near perfectly lattice matched substrate, $LiNbO_3$ and $LiTaO_3$. Georgia Tech's previous experience with the growth on these substrates includes a patented application for growth of GaN based transistor structures for direct electrical drive of optoelectronic modulators (US patent 7,173,286, Semiconductor devices formed of III-nitride

compounds, lithium-niobate-tantalate, and silicon carbide). Furthermore, Georgia Tech will explore a stack of epitaxially sandwiched piezoelectric/magnetostrictive layers in an attempt to create a low loss RF multiferroic that maintains rigidity necessary for high frequency operation while minimizing eddy current loses in a manner akin to laminated transformer housings commonly performed at lower frequencies and larger dimensions. The technology will have the following specific advantages:

- Strongest predicted high frequency piezoelectric/magnetostriction coupling coefficients
- Very high (highest practical) mechanical coupling coefficients through the use of $LiNbO_3$ and/or $LiTaO_3$
- High frequency mechanical compatibility by using the most rigid available magnetostrictive material, Terfenol-D
- Single crystalline design will amplify material properties including:
    - Highest domain order possible via a-axis lattice matched substrate/Terfenol
        - Terfenol $a \approx 5.189$ and $c \approx 12.82$ Å
        - $LiNbO_3$ has $a \approx 5.15$ and $c \approx 13.86$ Å
        - $LiTaO_3$ has $a \approx 5.154$ and $c \approx 13.73$ Å
        - Above choices insure compressive strain "preload" necessary for optimal magnetostrictive/piezoelectric coupling.
    - Strain and magnetostriction tunability through use of varying substrate lattice constants and thermal expansion mismatch.
        - Both bulk substrates and epitaxial $LiNbO_3$ will be explored. The use of epitaxial $LiNbO_3$ expands available thermal mismatch materials to include substrates of sapphire (Al_2O_3) and SiC and offers lower substrate dielectric constants useful for RF applications and better power handling capabilities (SiC).
- The developed materials will be examined via RF transmission line measurements as a function of growth substrate and growth condition to optimize the high frequency operation of the multiferroic materials.
- The developed materials will be used in parametric amplifiers.

The original approach for Terfenol-D film growth showed serious implementation Flaws:

- Approach:
  - 4-simultaneous Electron Beam Evaporators added to MBE system
  - Would have added doped Terfenol-D capability to existing piezoelectric MBE system
- Advantages:
  - Nearly unlimited growth rate allowing both thin and thick films
  - All materials deposited in the same chamber
- Disadvantages:
  - Stoichiometry control would have been difficult
- Road Block:
  - Dry runs before ordering indicated the potential for melting the vacuum system walls due to insufficient e-beam to chamber clearance.
- Action:
  - Vendor could not miniaturize system enough to avoid melting the vacuum system so alternative implementation developed.

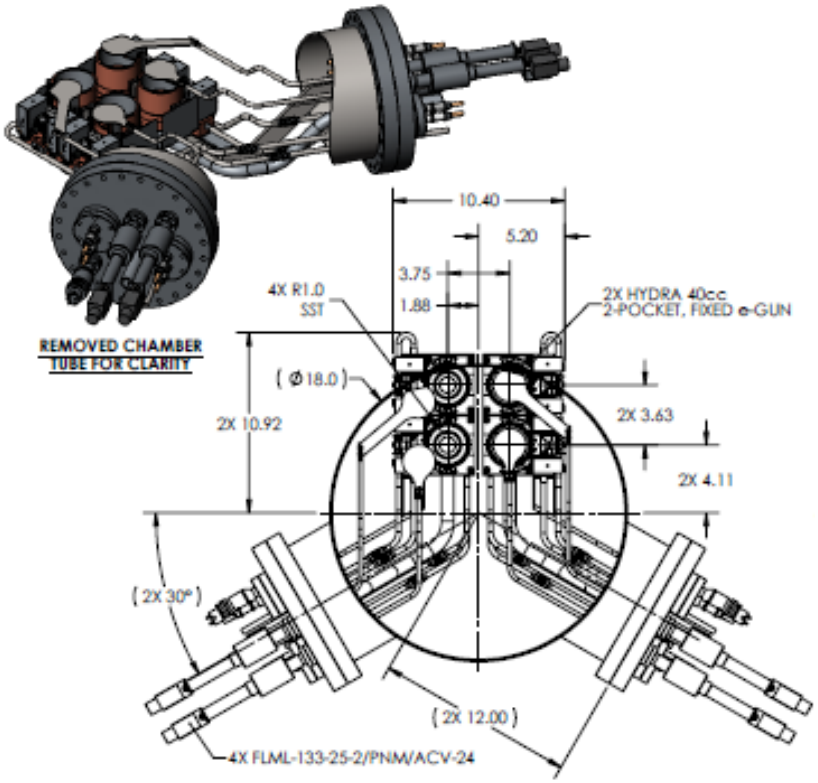

Figure 2.2: Original materials growth system

As a result of the issues just described a new approach was attempted:

- Convert a “Reserve MBE” to Dedicated Metals Epitaxy.
  - Represents an additional unplanned ~$500K investment by Ga Tech
- Piezoelectric Materials to be deposited in separate Chamber.
- Requires Vacuum transfer between layers
- Advantages:
  - Significantly higher control of stoichiometry including use of an in situ Auger chemical analysis tool exclusive to Ga Tech and newly acquired (different program) surface characterization toolsets
  - Faster delivery of parts
  - Faster overall development time

- Disadvantages:
  - Limited to thinner films due to limited deposition rate (still sufficient)
  - Slower structure rates due to the slower deposition rates and need for interlayer vacuum transfer.

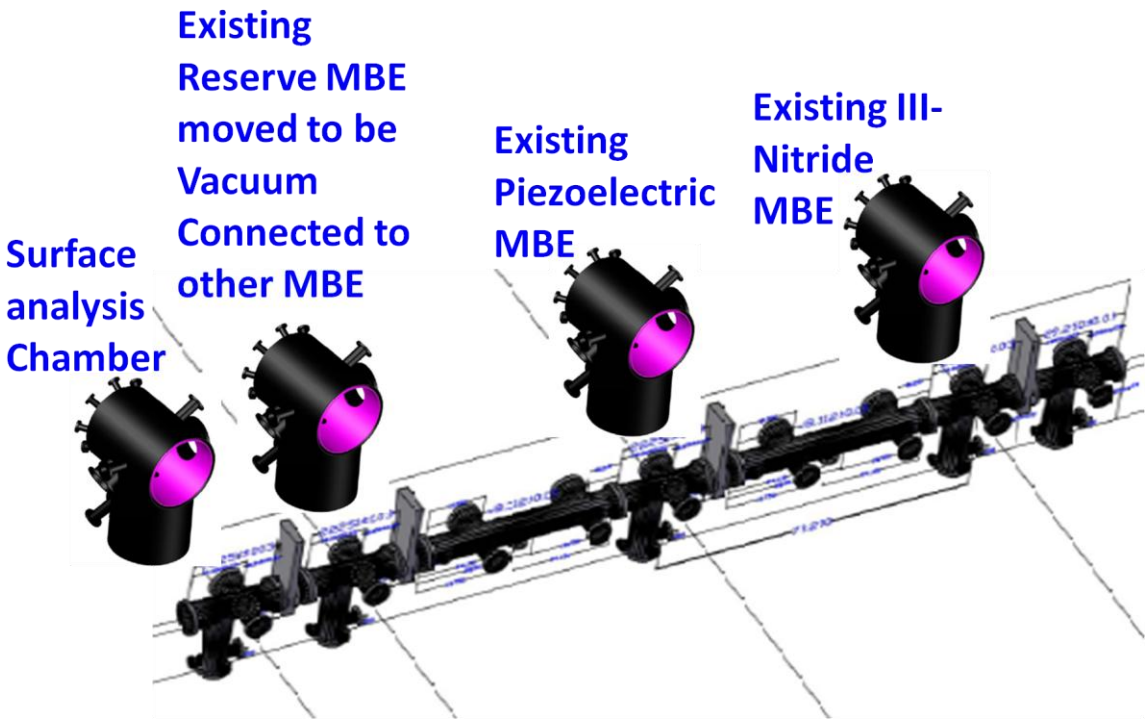

Figure 2.3: New materials growth system.

Materials –Problems with Tb deposition–Problem with O2contamination improving, but still there–Al cap to prevent post-growth Fe oxidation works well

Demonstrated growth of Terfenol-D
•Previously (Oct 2010) plagued by post-growth oxidation
•Saw small hysteresis in B-H measurements
•Found traditional composition control difficult due to lack of SIMS standards and previously unexplained anomalies in the flux measurements (perhaps now understood –see later details)
•Improvements Relative to October 2010 Review
•Added an Aluminum cell to cap samples to prevent post growth oxidation
•SIMS analysis shows capping greatly reduced oxygen content in Fe, and Dybut not in Tb
•TbO(and slight DyO) impurities are clearly from the effusion cell NOT post growth. This contamination is found to be the reason for minimal magnetic properties
•Future work includes:
•Eliminate TbOcontamination
•Growth under closed loop feedback control using SAP chemical probe
•Growth on lattice matched LiTaO3piezoelectric
•Testing of magnetic properties of proper stoichiometry films
•B-H measurements under applied electrical bias

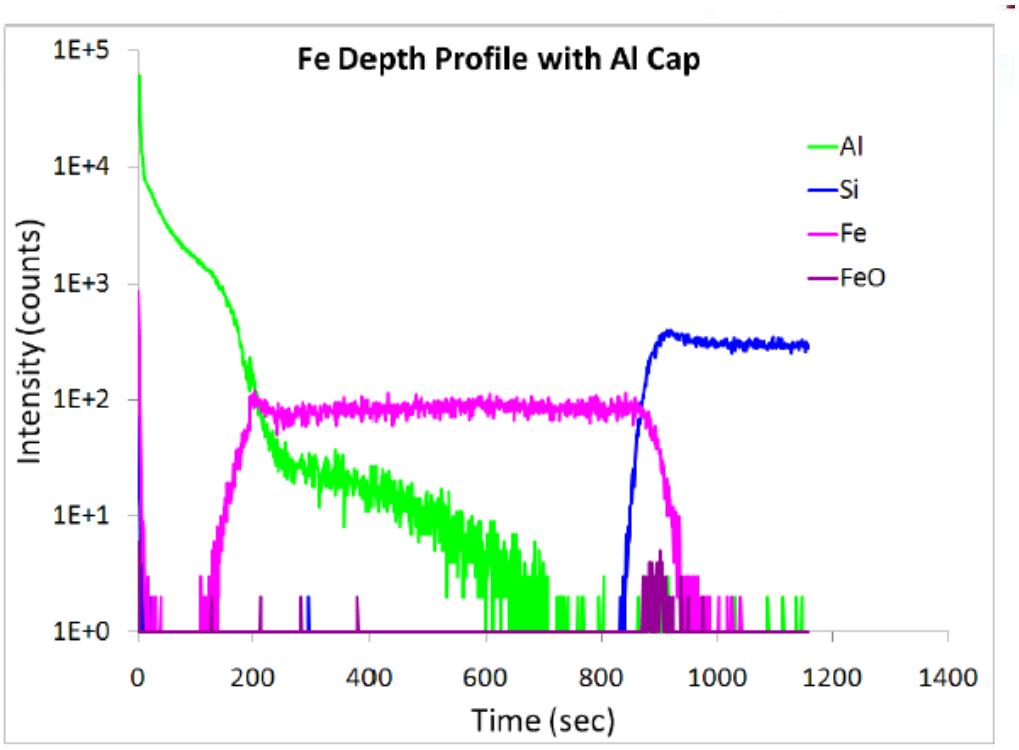

Figure 2.4: Iron depth profile with aluminum cap.

Al cap eliminated Fe oxidation. Generally proves that any oxygen detected no longer comes from post growth atmosphere exposure

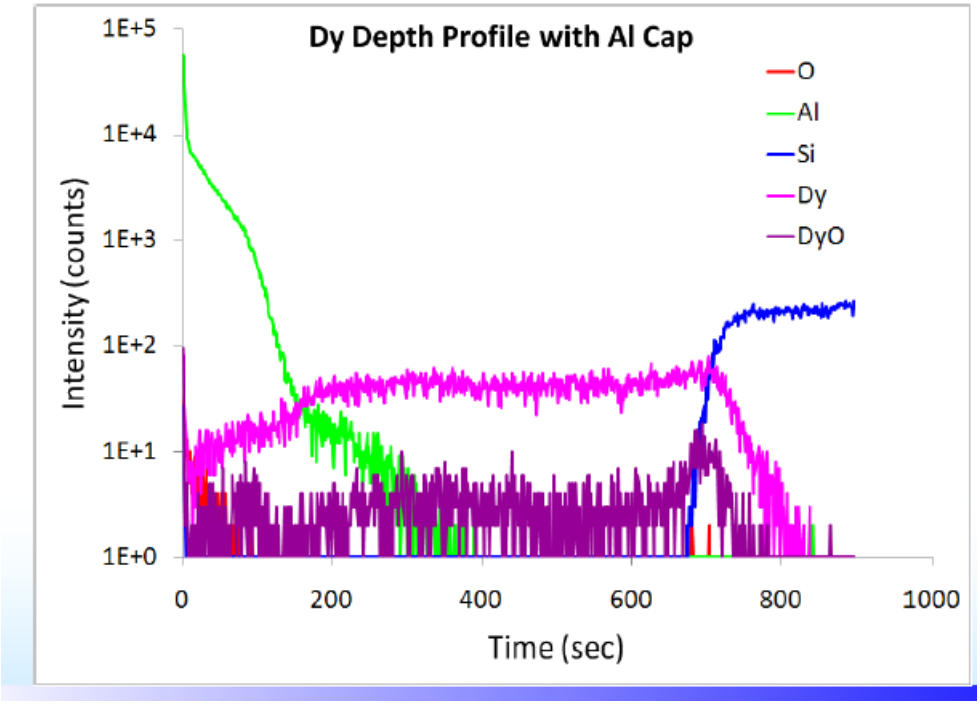

Figure 2.5: Dysprosium showing minimal "during growth" oxygen contamination and no "postgrowth" oxidation due to Al Cap

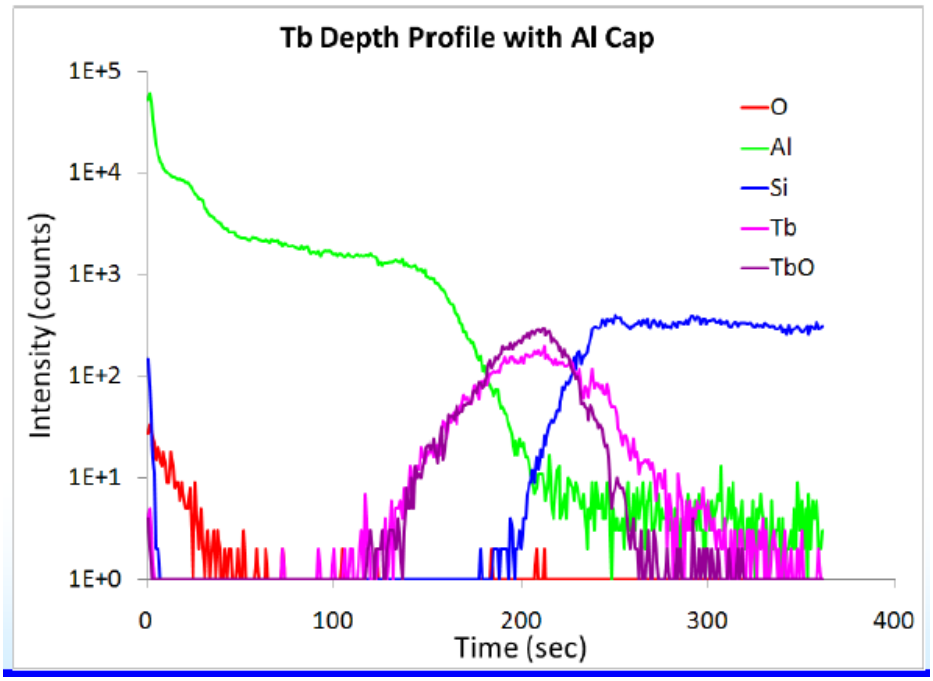

Figure 2.5: Terbium shows enormous "during growth" oxygen contamination.

After loading, Tb was found to **catalyze the decomposition of H2O** resulting in an enormous gaseous oxygen out gassing and resulted in substantial TbO source contamination
•Presently this TbO is also thought to be the reason for :
•…the **erratic flux measurements** (due to deposition of an insulator , TbO, on the ion gauge collector)
•… the **drift in deposition rates** as the TbO cap evaporates exposing underlying pure Tb
•Suggested solution to the TbO contamination is:
•H fetch source material in a dry box and load under dry conditions to avoid moisture introduction
•If contamination continues attempt a vacuum re-melt of Tb
•Potentially could damage the effusion cell since molten Tb "may" react with the crucible resulting in a potential punch through of molten Tb that could flow into the electrical part of the cell causing catastrophic damage.

D. In situ Auger Electron Analyzer System Employed for MBE Trace Element Analysis of Terfenol-D

Auger Electron Spectroscopy (AES) is a surface sensitive analysis technique used to identify elemental composition and determine chemical bonding. Typically AES is an *ex situ* technique with the exception of a few custom implementation. A prototype Staib *In situ* Auger Probe's (SIAP) surface sensitivity is quantified by depositing Tb onto a layer of Dy and Dy onto a layer of Tb in 0.01 monolayer increments. The prototype is able to distinguish surface coverage changes as small as 2% of a monolayer when elements with similar Auger spectra are used. The SIAP also allowed the identification of three different contributors to residual oxygen contamination in the system including the Tb source itself.

The SIAP was installed to characterize and monitor the stoichiometry of films grown in an MBE system configured to grow Terfenol-D, $Tb_xDy_{1-x}Fe_2$, the most magnetostrictive material known . This is a challenge for any Auger probe since AES is less sensitive to heavier elements [**Error! Bookmark not defined.**] and Tb and Dy are neighbors in the lanthanide series. Furthermore, to maximize the magnetostrictive properties of Terfenol, a completely miscible alloy of $TbFe_2$ and $DyFe_2$, a ratio of 28% Tb to 72% Dy must be maintained. Any deviation from that ratio results in a sharp reduction in the Terfenol's magnetostrictive properties. Initially the probe's surface sensitivity was quantified by depositing Tb on a Dy layer and Dy on a Tb layer in 0.01 monolayer increments. It was determined by XPS that the first Terfenol growth attempts in this system showed substantial oxygen contamination, so the SIAP was used to determine the sources of the oxygen.

The ASE spectra were taken in a Varian Gen II MBE system during or after film growth. The Auger probe was positioned normal to the sample with a working distance between 50 and 82 mm and used two separate sources of primary electrons. A Near-Normal Electron-gun (NNE) in one of the cell ports was used to provide near-normal incidence electrons and a RHEED gun was used as a grazing incidence electron source. Tb, Dy, and Fe were delivered by high temperature MBE Komponenten effusion cells and Al was delivered by a cold-lipped 40cc Veeco effusion cell, for capping the films. Figure 2.6 shows a diagram of the chamber and the position of the critical components. All growth materials were loaded under atmosphere and all growths were performed on Si (1 1 1) substrates near room temperature after RCA cleaning. *Ex situ* characterization included thickness measurements with a Tencor Alpha-Step Profilometer for growth rate calibration. A Thermo K-Alpha XPS was used to characterize the initial Terfenol growths. An IonTOF ToF-SIMS was used to obtain depth profiles on latter growths to investigate the oxygen contamination in the films. In all SIMS measurements the Cs sputter beam was employed to prevent oxygen contamination when obtaining depth profiles. COMPRO was used for Auger reference lines and comparison spectra and the Thermo Scientific Avantage Data System was used in peak identification of XPS data.

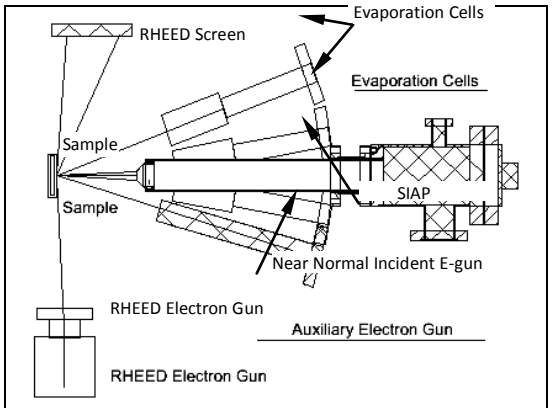

Figure 2.6. A diagram of the experimental setup on the GEN II MBE system.

Results and Discussion

The probe was initially calibrated by depositing a thin layer of each Terfenol growth component separately. Tb, Dy, and Fe were deposited at Beam Equivalent Pressures (BEP) of 3.6×10^{-9}, 4.2×10^{-9}, and 2.0×10^{-8} Torr respectively. Figure 2.7 shows the measured spectra after deposition.

In order to quantify the SIAP's sensitivity to surface changes the Tb and Dy sources were used. These elements were chosen since Auger is less sensitive to heavier elements and because their most distinguishable Auger lines, MNN, partially overlap. Initially a layer of pure Dy was deposited. Then, using a Tb flux of 1.2×10^{-9} Torr BEP, Tb was deposited in 0.01

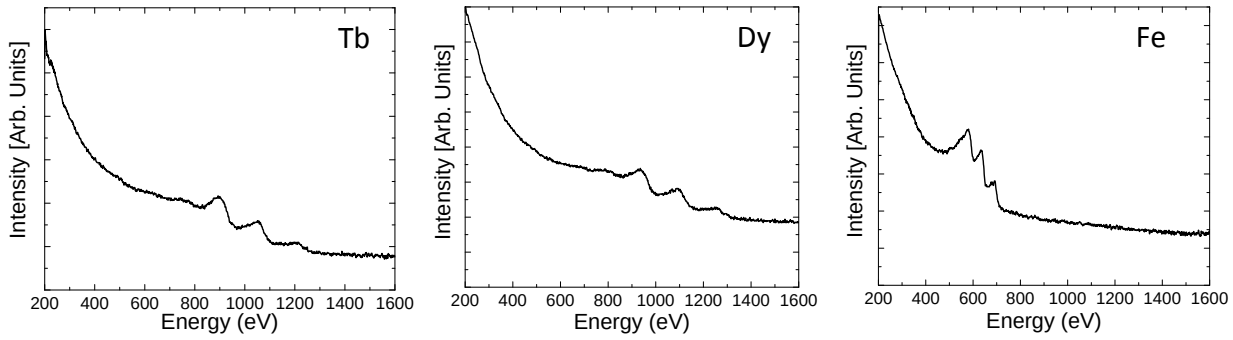

Figure 2.7. Initial spectra of each Terfenol component, from left to right Tb, Dy, and Fe.

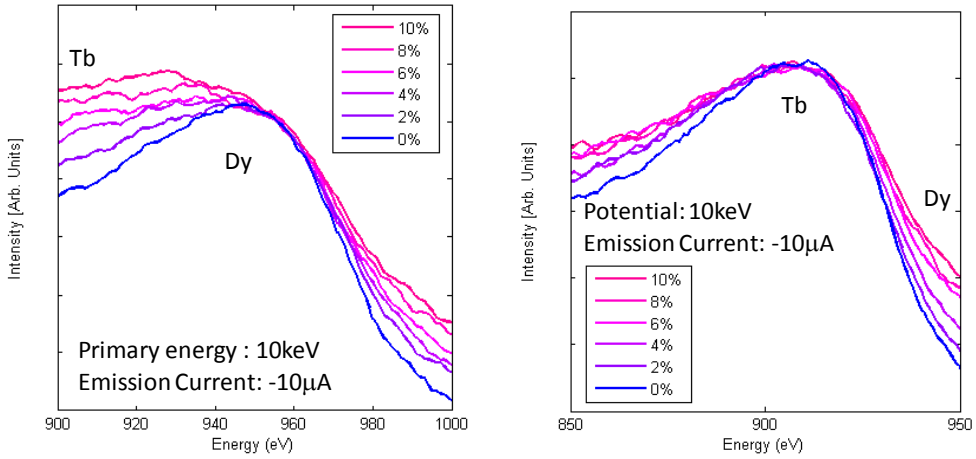

Figure 2.8. Auger spectra of a Dy layer transitioning to 10% of a monolayer of Tb coverage (left) and a Tb layer covered to 10% of a monolayer with Dy (right) at 2% increments. Data is normalized just to the right of the Dy peak (left) and at the Tb peak (right). The black bar indicates the expected location of the Auger peak of the material being deposited.

monolayer doses. Later a layer of Tb was deposited and, using a flux of 1.1×10^{-9} Torr BEP, Dy was deposited in 0.01 monolayer doses. The percent monolayer coverage was calculated by a standard impingement rate equation. Figure 2.8 shows the transition in the Auger spectra as the Dy surface is covered with Tb (left) and the Tb surface is covered with Dy (right) in 2% of a monolayer increments, up to 10% coverage. As Tb is deposited the peak shifts left towards the Tb MNN peak while Dy deposited on a Tb layer results in an increase in signal near the Dy MNN peak position. This demonstrates the SIAP's ability to detect changes in surface chemistry even when elements have similar Auger spectra. The SIAP was then used to identify the sources of oxygen contamination present in the system.

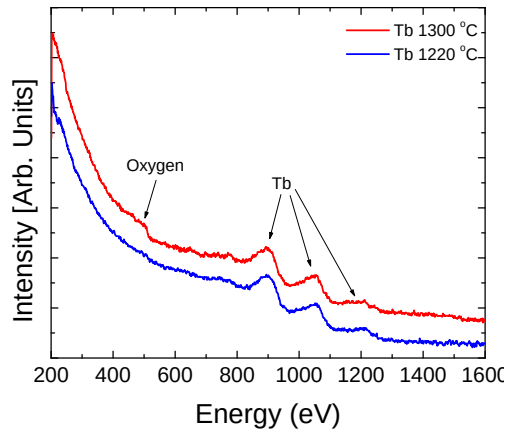

Figure 2.9. Terbium grown at 1220 °C does not show a noticeable level oxygen contamination (bottom) but oxygen is detected in the film grown at 1300 °C (top).

XPS analysis of films grown in the test system revealed an abundance of oxygen in initial terfenol growth attempts shown in Figure 2.9 below. The SIAP was employed to determine the sources of oxygen. Three sources of oxygen were identified. The chamber had a high enough partial pressure of oxygen to oxidize the Tb. Initially Tb was deposited and immediately AES spectra was taken using each electron source. The spectra were then retaken after 30 hours. Figure 2.10 shows the resulting spectra. The initial spectrum generated with the NNE gun only shows Tb lines while the initial spectrum taken with the RHEED gun also shows a small oxygen line. This increase in sensitivity is due to higher surface and near-surface Auger generation resulting in more Auger electrons that can escape the surface and be captured. After 30 hours both spectra exhibited an oxygen line

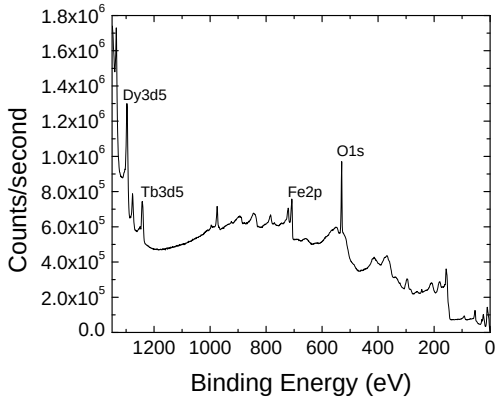

Figure 2.9. XPS spectra of a Terfenol-D growth exhibiting a high concentration of oxygen.

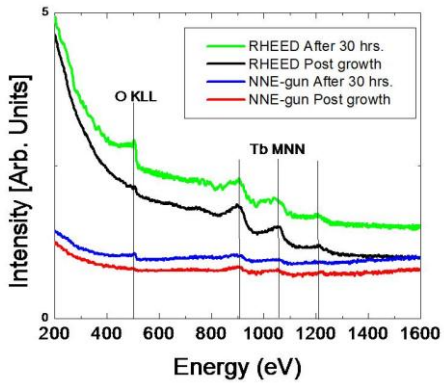

Figure 2.10. Auger spectra of the Tb before and after 30 hours in the growth chamber taken with both e-guns. From top to bottom: RHEED post 30 hours and post growth, near normal e-gun post 30 hours and post growth.

and the RHEED generated spectra exhibits a decrease in the Tb to O ration from 6:1 to 2:1 proving the partial pressure of oxygen in the chamber is oxidizing the Tb. Further analysis of the NNE gun generated spectrum after 30 hours shows a Tb to O ratio of 5:1 due to deeper film penetration, resulting in a higher Auger electron generation rate below the surface when the NNE gun is employed, further confirming a concentration of oxygen at the surface. However, since the post growth RHEED generated spectrum showed oxygen it was likely there were other sources of oxygen.

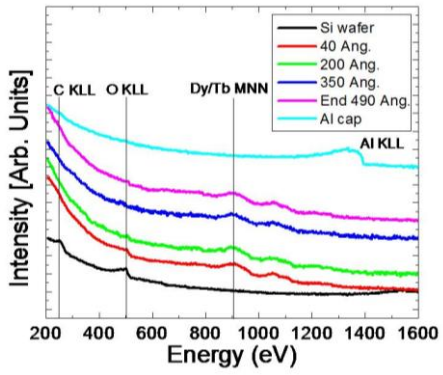

Figure 2.11. Auger spectra of the Tb/Dy alloy before growth is initiated until capped with Al from bottom to top.

The Tb charge was also a source of oxygen. When each component of Terfenol was deposited at growth level fluxes, 3.9×10^{-8} Tb, 8.3×10^{-8} Dy, 7.9×10^{-8} Fe, only Tb exhibited an oxygen line. Figure 2.10 shows Tb grown at 2 different fluxes, 7.2e-9 and 3.9e-8 Torr BEP. The higher flux, resulting from higher cell temperature, shows a strong oxygen line. The presence of oxygen was confirmed with SIMS. Figure 2.11 shows each material deposited at growth level fluxes and capped with Al to prevent *ex situ* oxidation. The SIMS data shows a high oxygen concentration in the Tb while Dy and Fe exhibit little to no oxygen. However, the SiO_2 layer on the Si substrate is also a source of oxygen in all the films, as demonstrated by an increase in the oxide signal at the Si/metal interface in all 3 SIMS plots.

The SIAP was then employed to determine if oxygen from the SiO_2 interface was intermixing with the films. A target alloy of Tb 29% and Dy 71% was grown at 490 Å/hr and monitored by the SIAP during growth (Figure 2.12). Initially two surface contaminates are detected prior to growth, C and O, since the sample was not outgassed. While the carbon line is not detected after 40 Å of growth the oxygen line is detected after 200 Å of deposition indicating intermixing with the oxygen at the SiO_2 interface. The results are shown in Figure 2.12

In conclusion, The SIAP is an MBE compatible Auger probe that can detect trace elements to 2% of a monolayer coverage even in the case of neighboring elements with partially overlapping Auger peaks, a challenge for any Auger system. The prototype is a quantitative growth monitoring tool for MBE. This is especially useful when working with films without line compositions. The SIAP was also an invaluable resource in detecting sources of contamination in this MBE system. In the future, the SIAP, coupled with a future closed loop control system, may enhance growth of films with multiple oxidation states or other similar phase/chemical transitions. MBE growers have long relied on qualitative data from RHEED to monitor changes in the surface crystal structure of growing films. Now the SIAP can add real time quantitative chemical analysis to MBE, complimenting RHEED.

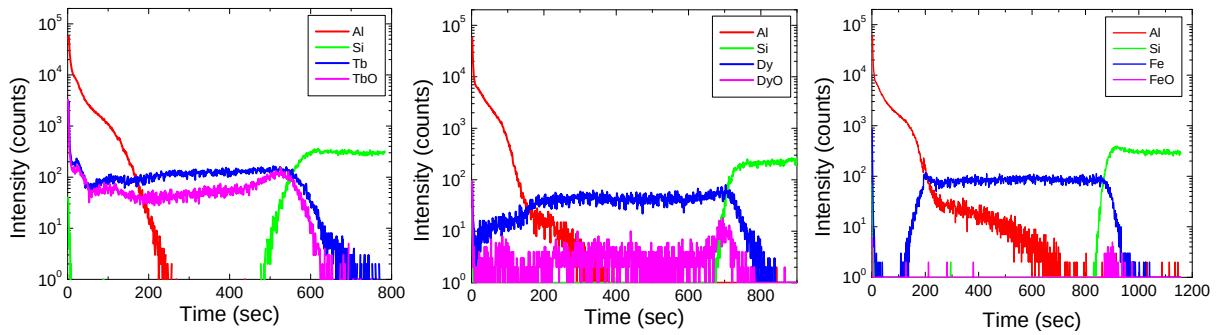

Figure 2.12. A SIMS depth profile of each Terfenol component grown on Si and capped in Al, from left to right: Tb, Dy, Fe.

3. Tunable Transmission Line Device Development

A) Transmission Line Test Structure

In order to evaluate the relative change due to permeability change, simulations were performed on a coplanar waveguide (CPW) stucture on a Lithium Niobate substrate as shown below.

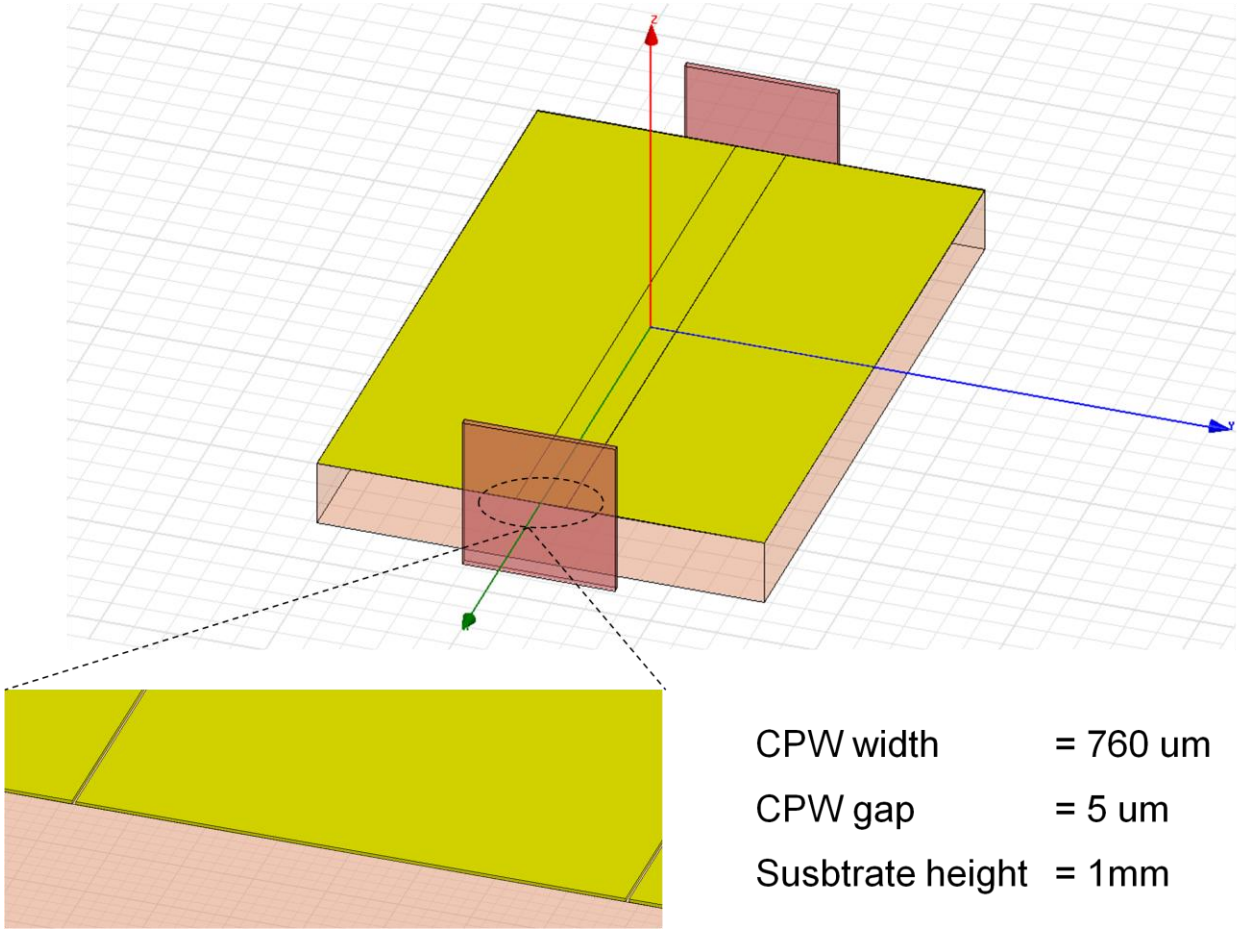

Figure 3.1: Tunable transmission line device model

B) Simulation Studies

We used aluminum as a test case and compared the variation to Terfenol-D. As shown in the figure below, the relative shift in phase velocity at 3 GHz of alumimum was shown to be zero, as its permeability does not change. In contrast, the Terfenol-D CPW transmission line showed shifts of 1.44:1 as μ_r ranged from 2 to 10 (our best estimate of the material response). A second simulation was performed at 5 GHz which showed a similar change in phase velocity. In both cases, the change in phase velocity attributed to the shift in permeability (i.e. keeping permitivity constant) was typically about 10% of the total 44% change. More of the change was attritubuted to the change in permitivity of the piezoelectric lithium niobate.

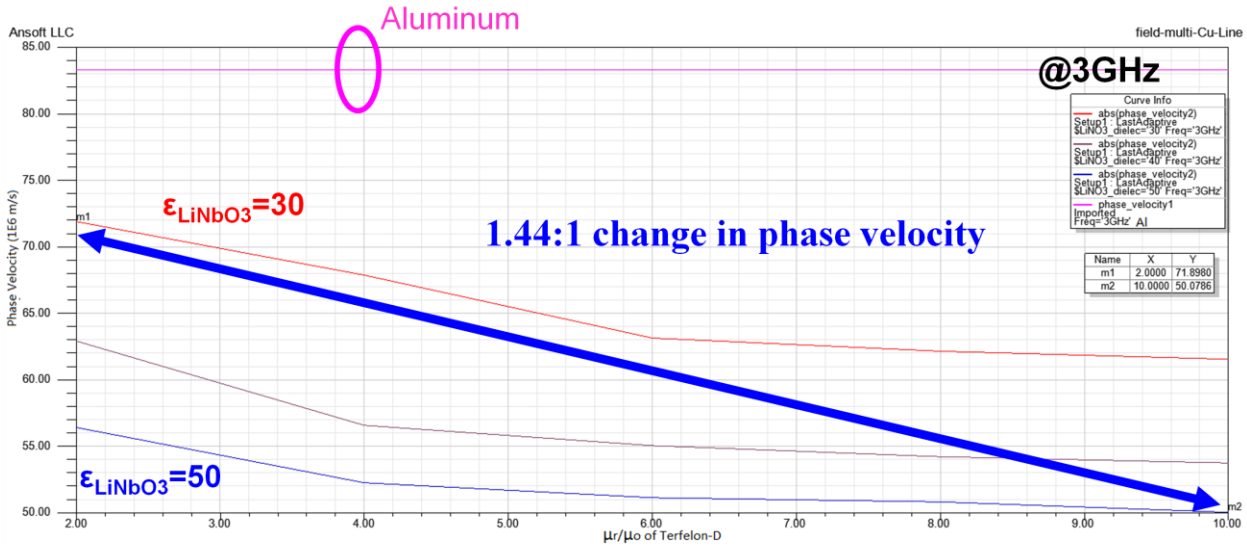

With the relative permittivity changed from 30 to 50 and compared the results with the CPW made by Al

Figure 3.2: Phase velocity change of Terfenol-D CPW line.

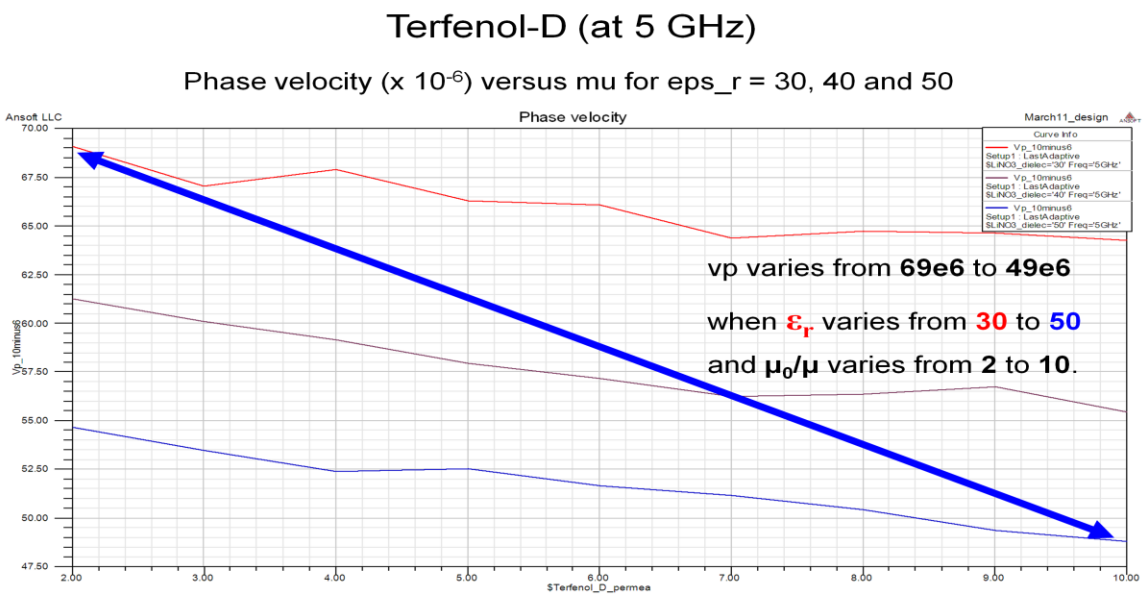

Figure 3.3: Terfenol-D CPW at 5 GHz.

4. Parametric Amplifier Circuit Development

A) Theory of Parametric Amplifiers

Parametric amplification is a process of RF-RF power conversion that operates by pumping a nonlinear reactance with a large-signal RF pumping source to either produce mixing products with gain or to generate a negative resistance. Parametric amplifiers (paramps) were traditionally grouped into two types: the phase-incoherent upconverting parametric amplifier and the negative-resistance parametric amplifier. With phase-incoherent upconverting parametric amplifiers, a fixed-frequency phase-incoherent incommensurate pump, at frequency f_p, mixes with an RF small-signal source input, at frequency f_s, to produce an upconverted output with gain that can be predicted by the Manley-Rowe relations. Negative-resistance parametric amplifiers are also mixers, but differ from phase-incoherent upconverting paramps in that the frequency relationship $f_i = f_p - f_s$ must be satisfied, where f_i is the so-called ``idler'' frequency. The Manley-Rowe relations show that negative-resistance parametric amplifiers present a regenerative condition with the possibility of oscillation at both the source and idler frequencies.

B) The Manley-Rowe Relations

In 1956, J. M. Manley and H. E. Rowe published a manuscript that analyzed the power flow into and out of a nonlinear reactive element under excitation at its different harmonic frequencies. The results of this analysis were two simple mathematical expressions quantifying how the total outgoing power flow would distribute itself among the harmonic terms. These two mathematical relationships, which will now be referred to as the Manley-Rowe relations, have the following important properties:

1. They are independent of the particular shape of the capacitance-voltage or inductance-current curve for a nonlinear capacitance or nonlinear inductance, respectively.

2. The power levels of the various driving sources are irrelevant.

3. The external circuitry connected to the nonlinear reactance will not affect how the power is distributed to the harmonic frequencies.

These two expressions provide information pertaining to the ideal performance metrics (such as gain and stability) of nonlinear reactance mixers and amplifiers without prior knowledge of the reactive devices or their surrounding circuitry. Because of the impact of the Manley-Rowe relations to parametric amplifiers, a shortened derivation will be presented here with an analysis of their applications to parametric amplifiers and mixers.

Manley and Rowe began their analysis by considering a circuit similar to that in Fig. 4.1. Figure 4.1 contains two voltage sources, V_1 and V_2, at frequencies f_1 and f_2, with their associated generator impedance, Z_o. These two voltage sources are electrically isolated from one another through ideal bandpass filters that are assumed to pass their indicated

frequencies, and provide an open-circuit out-of-band. The two sources are placed across a nonlinear capacitance (though Manley and Rowe state that their derivation could have proceeded using a nonlinear inductance instead) whose capacitance, $C(V)$, is a function of its own terminal voltage V. In addition to the two voltage sources, an infinite number of resistive loads have been connected across the nonlinear capacitor, each electrically isolated from the rest of the circuit by an ideal bandpass filter. The passband frequency of each load bandpass filter has been selected to correspond to a specific harmonic combination of the two driving frequencies, f_1 and f_2, that occur because of the nonlinear mixing action of the nonlinear capacitance. Manley and Rowe made the assumption that the driving frequencies were incommensurate such that the ratio of the two will always satisfy

$$\frac{\omega_1}{\omega_2} \notin \mathrm{Q}. \tag{4.1}$$

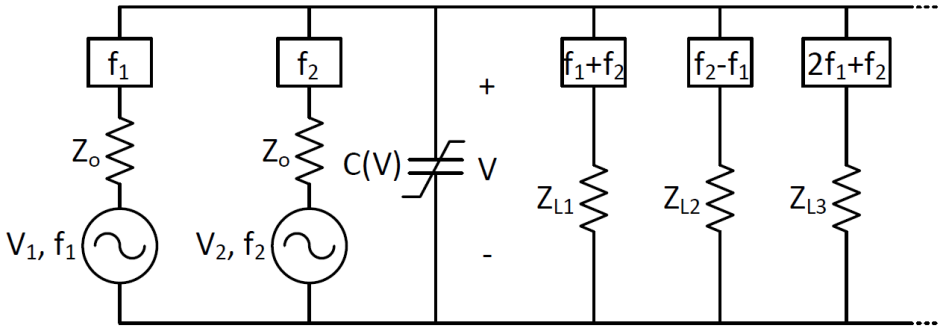

Figure 4.1: Simplified circuit model that Manley and Rowe considered for their derivation.

To begin the derivation, consider that the total charge, q, flowing into and out of the nonlinear capacitor in Fig. 2 can be expressed as a two-dimensional Fourier series as

$$q = \sum_{n=-\infty}^{\infty} \sum_{m=-\infty}^{\infty} q_{m,n} e^{j(m\omega_1 + n\omega_2)t}, \tag{4.2}$$

where the charge series coefficients, $q_{m,n}$, are expressed as

$$q_{m,n} = \frac{1}{4\pi^2} \int_{-\pi}^{\pi} \int_{-\pi}^{\pi} V \times C(V) e^{-j(mx+ny)} dxdy, \tag{4.3}$$

with $x = \omega_1 t$ and $y = \omega_2 t$. The total current, $I_{m,n}$, through $C(V)$ is the total time derivative of the charge series coefficients,

$$I_{m,n} = \frac{dq_{m,n}}{dt} = \frac{\partial q_{m,n}}{\partial t} + \frac{\partial q_{m,n}}{\partial \omega_1}\frac{d\omega_1}{dt} + \frac{\partial q_{m,n}}{\partial \omega_2}\frac{d\omega_2}{dt}. \tag{4.4}$$

However, the incommensurability of ω_1 and ω_2 causes $\frac{\partial q_{m,n}}{\partial \omega_1} = \frac{\partial q_{m,n}}{\partial \omega_2} = 0$. As a result, (3.5) reduces to the partial time derivative of the charge series terms

$$I = \frac{\partial q}{\partial t} = \sum_{n=-\infty}^{\infty}\sum_{m=-\infty}^{\infty} I_{m,n} e^{j(m\omega_1 + n\omega_2)t} \tag{4.5}$$

$$I_{m,n} = j(m\omega_1 + n\omega_2)q_{m,n}. \tag{4.6}$$

The voltage across the nonlinear capacitor, V, may also be expressed as a two-dimensional Fourier series, just as was done with the charge,

$$V = \sum_{n=-\infty}^{\infty}\sum_{m=-\infty}^{\infty} V_{m,n} e^{j(m\omega_1 + n\omega_2)t}, \tag{4.7}$$

where the voltage series coefficients can be expressed as

$$V_{m,n} = \frac{1}{4\pi^2}\int_{-\pi}^{\pi}\int_{-\pi}^{\pi} V e^{-j(mx+ny)} dxdy. \tag{4.8}$$

It is at this point in their derivation that Manley and Rowe performed some mathematical "sleight-of-hand" in order to form products of $I_{m,n}$ and $V_{m,n}$ to obtain power series coefficients, $P_{m,n}$. The tricks employed by Manley and Rowe involves separating the problem into two parts, dealing first with frequencies at f_1 corresponding to index m, then next with frequencies at f_2 corresponding to index n, and do not need to be reproduced here; what is important is the result of this mathematical manipulation,

$$\sum_{m=-\infty}^{\infty}\sum_{n=-\infty}^{\infty}\frac{mV_{n,m}I_{n,m}^*}{mf_1 + nf_2} = \sum_{m=0}^{\infty}\sum_{n=-\infty}^{\infty}\frac{m2\Re\{V_{n,m}I_{n,m}^*\}}{mf_1 + nf_2} = \sum_{m=0}^{\infty}\sum_{n=-\infty}^{\infty}\frac{mP_{n,m}}{mf_1 + nf_2}, \tag{4.9}$$

where $P_{n,m}$ is the power flowing either into or out of the nonlinear capacitor at frequency $nf_1 + mf_2$. The desired result for the power flow through a nonlinear reactance is thus, by Conservation of Energy,

$$\sum_{m=0}^{\infty}\sum_{n=-\infty}^{\infty}\frac{mP_{n,m}}{mf_1 + nf_2} = 0. \tag{4.10}$$

When concerned with the evaluation of the power flow in a nonlinear reactance with respect to index n, a second result can be obtained.

$$\sum_{n=0}^{\infty}\sum_{m=-\infty}^{\infty}\frac{nP_{n,m}}{mf_1+nf_2}=0 \tag{4.11}$$

Equations (4.10) and (4.11) are known as the Manley-Rowe relations.

As discussed above, the Manley-Rowe relations are independent of the shape of the capacitance-voltage or inductance-current curve of the nonlinear reactance and the nature of the surrounding circuitry, assuming proper isolation of driving and harmonic currents. As a result, the Manley-Rowe relations provide a way to quantify the idealized metrics of parametric systems, such as gain and stability, and thus a figure of merit to evaluate the performance of circuit designs.

To illustrate this concept, let the voltage generator $V1$ in Fig. 2 be a small-signal input source, and $V2$ be a large-signal pumping source that is required to drive the nonlinear action of the nonlinear capacitor. Consider that power is allowed to flow out of the nonlinear reactance at a frequency $f_3 = f_1 + f_2$. Then (4.10) and (4.11) reduce to

$$\frac{P_1}{f_1}+\frac{P_3}{f_3}=0 \tag{4.12}$$

$$\frac{P_2}{f_2}+\frac{P_3}{f_3}=0. \tag{4.13}$$

To satisfy Conservation of Energy, we will define power flowing into the nonlinear capacitance as positive, and power flowing out of the nonlinear capacitance as negative. By rearranging (4.12) and (4.13), a gain expression can be obtained that is the ratio of output power to input power when power extracted at f_3 is considered to be the desired output term.

$$gain=\frac{f_3}{f_1} \tag{4.14}$$

Equation (4.14) demonstrates that given both lossless components and ideal harmonic isolation and terminations the maximum gain that is achievable when using a parametric circuit to upconvert a signal from a frequency f_1 to a frequency f_3 is the ratio of the upconverted frequency to the input frequency.

Conversely, let the signal frequency be equal to the sum of the desired output harmonic and the pumping frequency, such that now the signal frequency is f_3, the desired output frequency is f_1, and the pumping frequency remains at f_2. In this case, the parametric circuit is downconverting the input signal to a lower frequency and the Manley-Rowe relations predict the maximum achievable gain will be

$$gain = \frac{f_1}{f_3}, \tag{4.15}$$

which will always be less than one, or a loss.

The constraint of incommensurate frequencies imposed by Manley and Rowe in their derivation was challenged by Anderson and Someda. Their claim stems from reports of physically realized parametric circuits properly acting as upconverting parametric amplifiers when the ratio of the input to upconverted frequencies does not satisfy (4.1). When the driving generators are modeled as ideal, such that their driving voltage can be expressed as $V = V_o e^{j\omega t}$, then the constraint of incommensurate frequencies is necessary. However, nonideal physical generators cannot produce a discrete line spectrum. That is to say, the instantaneous output frequency of a physical generator is approximately ω, and will average out to ω over a sufficiently long time interval. The voltage of this physical generator could then be modeled as $V = V_o e^{j(\omega t + \phi)}$, where ϕ is some arbitrary phase that varies slowly over time with a mean value of zero. It is then arguable that the Manley-Rowe relations should be clarified to state that the instantaneous frequencies should be `almost always' incommensurate. Anderson demonstrated that in the statistical case when the frequencies become commensurate, ensuring phase incoherence of the driving sources maintains the validity of the Manley-Rowe relations.

C) Phase-Incoherent Upconverting Parametric Amplifiers

Three general properties define the operation of phase-incoherent upconverting parametric amplifiers: the output frequency is equal to the sum of the input source frequency and the pump frequency, power is allowed to flow only at the source, pump, and output frequencies, and the source and pump waveforms must maintain phase incoherence. As (4.14) demonstrated, the maximum upconverting gain is the ratio of the output frequency to the input frequency, and is achievable only when harmonic isolation is perfect and circuit components are ideal. In any physically realizable upconverting parametric amplifier, circuit component losses and leakage currents due to nonideal filters introduce mechanisms that limit approaching the ideal Manley-Rowe gain.

In an effort to better understand the operating characteristics of the phase-incoherent upconverting parametric amplifier, and to determine the primary circuit parameters responsible for decreasing the gain from the Manley-Rowe limit, Blackwell and Kotzebue considered a quasi-idealized circuit and developed an expression for the transducer gain of phase-incoherent upconverting parametric amplifiers based on the quality factor of the nonlinear reactance, frequencies of operation, and resistive terminations. To continue their work in identifying gain-limiting circuit and component characteristics, a similar circuit was explored, taking into account the capacitance range of the nonlinear capacitor.

Consider the circuit in Fig. 3 that contains an input small-signal source at frequency f_s and a large-signal pumping source at frequency f_p interacting with a voltage-dependent nonlinear capacitor, $C(v)$. Filters are in place to electrically isolate currents at the source and pump frequencies from the desired output mixing product $f_o = f_p + f_s$.

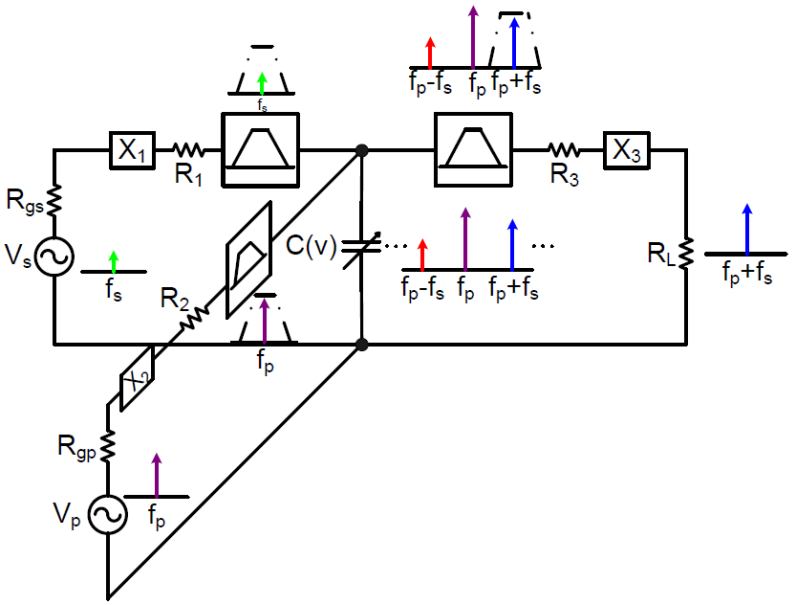

Figure 4.2: A phase-incoherent upconverting parametric amplifier.

Assuming that the pump voltage is several orders in magnitude larger than the source, the voltage across the reactive nonlinearity is dominated by the pump such that the voltage-dependent nonlinear capacitor can be considered a time-varying capacitance with frequency ω_p,

$$C(t) = C_o\left(1+2M\cos\omega_p t\right), \tag{4.16}$$

where M is proportional to the pump voltage and gives the coupling between the voltages at the two angular frequencies ω_s and ω_p, and C_o is the large-signal average capacitance of the nonlinear capacitor. Performing a derivation similar to Manley and Rowe, the power series coefficients can be expressed as

$$P_{n,m} = |I_{n,m}|^2 Z_{n,m}, \tag{4.17}$$

where $I_{n,m}$ and $Z_{n,m}$ are the current and impedance Fourier series coefficients of the nonlinear capacitance, respectively, and can mathematically be represented by

$$Z_{n,m} = \frac{1}{j\left(n\omega_s + m\omega_p\right)C_o\left(1+2M\cos y\right)} \tag{4.18}$$

$$q_{n,m} = \frac{1}{4\pi^2}\int_{-\pi}^{\pi}\int_{-\pi}^{\pi}\left(V_{dc} + V_s\cos x + V_p\cos y\right)$$

$$\times C_o\left(1+2M\cos y\right)e^{-j(nx+my)}dxdy \tag{4.19}$$

$$I_{n,m}=\frac{\partial q_{n,m}}{\partial t}, \tag{4.20}$$

where $q_{n,m}$ are the charge series coefficients, $y=\omega_p t$ and $x=\omega_s t$. For a phase-incoherent upconverting parametric amplifier, the power terms of interest are $P_{1,1}$, the power in the upconverted output signal, and $P_{1,0}$, the power in the source signal. Evaluation of (4.17) results in

$$\frac{P_{1,1}}{P_{1,0}}=G_o=\frac{\omega_s+\omega_p}{\omega_s}M^2=\frac{\omega_o}{\omega_s}M^2. \tag{4.21}$$

As we approach ideal conditions, M approaches unity, and we obtain the optimal gain predicted by Manley and Rowe.

Let us now assume that the time-dependent capacitance described by (4.16) is piecewise-linear, such that a sinusoidal excitation results in a sinusoidal change in capacitance. Let us also assume that the nonlinear capacitor's quality factor is sufficiently large such that its effects on the gain are negligible. Under these two assumptions, the coupling factor M can be treated as a constant and written as a direct function of the reactive nonlinearity's maximum and minimum capacitance, respectively C_{max} and C_{min}.

$$M=\frac{C_{max}-C_{min}}{C_{max}} \tag{4.22}$$

Substitution of (4.22) into (4.21) results in

$$G_o=\frac{\omega_o}{\omega_s}\underbrace{\left(1-2\left(\frac{C_{max}}{C_{min}}\right)^{-1}+\left(\frac{C_{max}}{C_{min}}\right)^{-2}\right)}_{1}. \tag{4.23}$$

Equation (4.23) represents the maximum obtainable small-signal gain given the available change in the reactive nonlinearities capacitance. This expression is limited to predicting only small-signal gain because of the assumption of a piecewise-linear capacitance-voltage curve. Term 1 in (4.23) can be considered a gain-degradation factor. Figure 4 shows the change in this gain-degradation factor with changing maximum-to-minimum capacitance ratio.

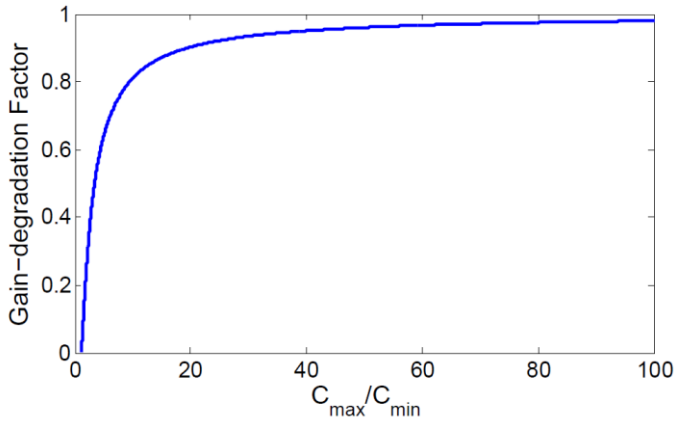

Figure 4.3: Change in term 1 in (4.23) with changing maximum-to-minimum nonlinear capacitance ratio.

From Fig. 4 it is clear that when assuming negligible circuit and component losses the gain of phase-incoherent upconverting parametric amplifiers approaches the Manley-Rowe limit as the nonlinear capacitor's available maximum-to-minimum capacitance ratio increases.

The bandwidth of phase-incoherent upconverting parametric amplifiers can be discussed if a couple of assumptions are first made. With respect to Fig. 3, the construction of the source, pump, and output filters was never specified. To determine a general expression for the bandwidth, these filters will each be comprised of high-Q series L-C resonant circuits. While single-tuned resonant circuits do not yield the maximum bandwidth, they do reduce the overall complexity of both the analysis and the corresponding mathematics.

Blackwell and Kotzbue approached the bandwidth of phase-incoherent upconverting parametric amplifiers in a similar manner. Their derivation showed that when a phase-incoherent upconverting parametric amplifier is optimized for maximum gain, the operating bandwidth, b, will be limited by

$$b \leq \frac{2}{Q_s}, \tag{4.24}$$

where Q_s is the loaded quality factor of the source L-C series resonant filter.

D) Negative-Resistance Parametric Amplifiers

Consider now the situation where power flows into the nonlinear reactance at both the small-signal source frequency and the large-signal pump frequency, and power flows out of the nonlinear reactance at the desired output, which is the difference between the pump and source frequency, $f_o = f_p - f_s$. In this case, the Manley-Rowe relations reduce to

$$\frac{P_o}{f_o} + \frac{P_p}{f_p} = 0 \tag{4.25}$$

$$\frac{P_s}{f_s} + \frac{P_p}{f_p} = 0. \tag{4.26}$$

Maintaining the power flow convention that positive power flows into the nonlinear reactance and negative power flows out, P_p must be positive. Therefore, to satisfy the equalities in (4.25) and (4.26), both P_s and P_o must be negative. That is, the nonlinear reactance is delivering power to the source signal generator at frequency f_s instead of absorbing power from it. If the gain of this system were to be defined as the ratio of power delivered to the source input from the nonlinear reactance to that being provided to the nonlinear reactance from the source input, then it is possible for infinite gain to occur, as (4.25) and (4.26) demonstrate that the nonlinear reactance is capable of delivering power to the source at frequency f_s whether or not the source input is active. The possibility of infinite gain suggests the potential for system instability at both f_s and f_o, however, when stable, this type of parametric amplifier has properties which differentiates it from the phase-incoherent upconverting parametric amplifier, and is known as a negative-resistance parametric amplifier. There are two modes of operation for negative-resistance parametric amplifiers: nondegenerate and degenerate.

Both degenerate and nondegenerate negative-resistance parametric amplifiers are considered single-frequency amplifiers since the input and output frequencies both occur at f_s. In addition, both modes satisfy the equality

$$f_o = f_p - f_s, \tag{4.27}$$

but since the output frequency is identical to the source frequency, two possibilities exist to fulfill (4.27). The first is when power flow is allowed to occur at a third frequency known as the "idler," f_i, such that $f_i = f_p - f_s$. In this case, the amplifier is designed so that the idler current is contained within the nonlinear reactance and is never delivered to a real load. By doing so, (4.27) is satisfied without the idler affecting the gain or efficiency of the amplifier. The second case is when the pump frequency is exactly twice that of the source, such that $f_i = f_p - f_s = 2f_s - f_s = f_s$. In the second case, the source and pump frequencies are harmonically related and the phase relationship between them directly affects amplifier performance.

a) Nondegenerate Negative-Resistance Parametric Amplifiers

Parametric amplifiers that satisfy (4.27) and $f_o = f_i \neq f_s$ are known as nondegenerate negative-resistance parametric amplifiers. The gain of these amplifiers is a function of the negative resistance that is created through the interaction of the source and pumping waves within the nonlinear reactance. Therefore, by determining an expression for the negative resistance of nondegenerate parametric amplifiers, an expression for the gain follows.

To begin the derivation, consider the nondegenerate parametric amplifier in Fig. 4.

Figure 5 contains a small-signal current source, $i_s(t)$, and a large-signal pumping source, $i_p(t)$, each with their respective generator conductances G_s and G_p. The load conductance, G_L, is located within the source circuit. Each independent source is electrically isolated from the other through the use of the high-Q resonant traps $L_s - C_s$ and $L_p - C_p$. The idler current is limited to circulate within the nonlinear capacitor, $C(v)$, through the use of the high-Q resonant trap $L_i - C_i$ such that no power is dissipated at that frequency.

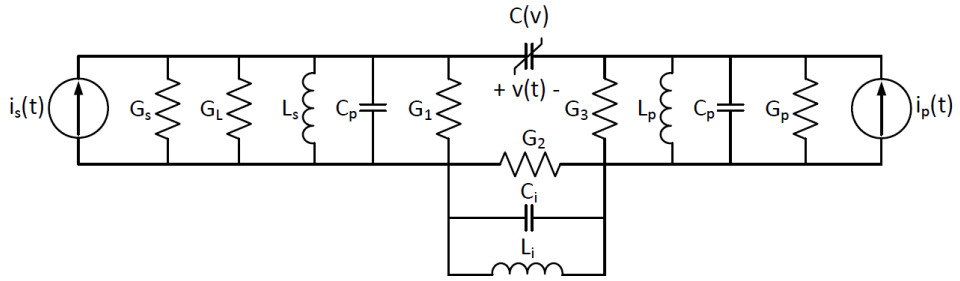

Figure 4.3: An equivalent circuit of a nondegenerate negative-resistance parametric amplifier.

Under the assumption that the sum of the source and pump voltage amplitudes are much smaller than the DC operating point, the charge, q, stored on the plates of the nonlinear capacitor can be expanded in a Taylor series about the DC operating point. If only the linear and quadratic terms of are sufficient size to consider in the expansion, then q can be written as

$$q = a_1 v(t) + a_2 v^2(t), \tag{4.28}$$

where $v(t)$ represents the total voltage across the nonlinear capacitor at frequencies f_s, f_p, and f_i,

$$v(t) = V_s \cos(\omega_s t + \phi_s) + V_i \cos(\omega_i t + \phi_i) + V_p \cos(\omega_p t + \phi_p), \tag{4.29}$$

and a_1 and a_2 are the Taylor series coefficients. V_s, V_i, and V_p in (4.29) are the peak values of the harmonic voltages making up the total voltage waveform $v(t)$. The linear term a_1 in the expansion in (4.28) must be well-defined, for to ensure high electrical isolation between source, idler, and pump currents, each resonant trap must satisfy

$$\omega_s = \frac{1}{\sqrt{L_s(C_s + a_1)}} \tag{4.30}$$

$$\omega_i = \frac{1}{\sqrt{L_i(C_i + a_1)}} \tag{4.31}$$

$$\omega_p = \frac{1}{\sqrt{L_p\left(C_p + a_1\right)}}. \tag{4.32}$$

With knowledge of the total charge stored on the plates of the nonlinear capacitor, the current passing through the nonlinear capacitor, $i_{NLC}(t)$, can be found from the nonlinear capacitor's C-V characteristics and the total voltage across its terminals.

$$i_{NLC}(t) = \frac{dq\left(v(t)\right)}{dv(t)}\frac{dv(t)}{dt} = C\left(v(t)\right)\frac{dv(t)}{dt} = a_1\frac{dv(t)}{dt} + 2a_2 v(t)\frac{dv(t)}{dt} \tag{4.33}$$

By substituting (4.29) into (4.33), expanding the result and grouping terms of similar frequency, the total current passing through the nonlinear capacitor can be expressed as

$$i_{NLC}(t) = i_s(t) + i_i(t) + i_p(t), \tag{4.34}$$

where

$$i_s(t) = -\omega_s a_1 V_s \sin\left(\omega_s t + \phi_s\right) - \omega_s a_2 V_i V_p \sin\left(\omega_s t + \phi_p - \phi_i\right) \tag{4.35}$$

$$i_i(t) = -\omega_i a_1 V_i \sin\left(\omega_i t + \phi_i\right) - \omega_i a_2 V_s V_p \sin\left(\omega_i t + \phi_p - \phi_s\right) \tag{4.36}$$

$$i_p(t) = -\omega_p a_1 V_p \sin\left(\omega_p t + \phi_p\right) - \omega_p a_2 V_s V_i \sin\left(\omega_p t + \phi_s + \phi_i\right). \tag{4.37}$$

Equations (4.35), (4.36), and (4.37) can now be rewritten as

$$i_s(t) = a_1\frac{dv_s(t)}{dt} + \frac{a_2 V_i V_p}{V_s}\left[\cos\left(\phi_p - \phi_i - \phi_s\right)\frac{dv_s(t)}{dt} - \omega_s v_s(t)\sin\left(\phi_p - \phi_i - \phi_s\right)\right] \tag{4.38}$$

$$i_i(t) = a_1\frac{dv_i(t)}{dt} + \frac{a_2 V_s V_p}{V_i}\left[\cos\left(\phi_p - \phi_i - \phi_s\right)\frac{dv_i(t)}{dt} - \omega_i v_i(t)\sin\left(\phi_p - \phi_i - \phi_s\right)\right] \tag{4.39}$$

$$i_p(t) = a_1\frac{dv_p(t)}{dt} + \frac{a_2 V_s V_i}{V_p}\left[\cos\left(\phi_p - \phi_i - \phi_s\right)\frac{dv_p(t)}{dt} + \omega_p v_p(t)\sin\left(\phi_p - \phi_i - \phi_s\right)\right]. \tag{4.40}$$

Taking the Fourier transform of (4.38), (4.39), and (4.40) and dividing each by their respective transformed voltage $\tilde{\mathbf{V}}_\mathbf{s}$, $\tilde{\mathbf{V}}_\mathbf{i}$, and $\tilde{\mathbf{V}}_\mathbf{p}$, the admittance of the nonlinear capacitor is obtained at the source, idler, and pump frequencies, $\tilde{\mathbf{Y}}_\mathbf{s}$, $\tilde{\mathbf{Y}}_\mathbf{i}$, and $\tilde{\mathbf{Y}}_\mathbf{p}$, respectively.

$$\tilde{\mathbf{Y}}_\mathbf{s} = \frac{\tilde{\mathbf{I}}_\mathbf{s}(\mathbf{j\omega j}}{\tilde{\mathbf{V}}_\mathbf{s}(\mathbf{j\omega j}} = j\omega_s a_1 + j\omega_s a_2\frac{V_i V_p}{V_s}e^{j\left(\phi_p - \phi_i - \phi_s\right)} \tag{4.41}$$

$$\tilde{\mathbf{Y}}_\mathbf{i} = \frac{\tilde{\mathbf{I}}_\mathbf{i}(\mathbf{j\omega j}}{\tilde{\mathbf{V}}_\mathbf{i}(\mathbf{j\omega j}} = j\omega_i a_1 + j\omega_i a_2\frac{V_s V_p}{V_i}e^{j\left(\phi_p - \phi_i - \phi_s\right)} \tag{4.42}$$

$$\tilde{\mathbf{Y}}_{\mathbf{p}} = \frac{\tilde{\mathbf{I}}_{\mathbf{p}}(\mathbf{j\omega j}}{\tilde{\mathbf{V}}_{\mathbf{p}}(\mathbf{j\omega j}} = j\omega_p a_1 + j\omega_p a_2 \frac{V_s V_i}{V_p} e^{-j\left(\phi_p - \phi_i - \phi_s\right)} \tag{4.43}$$

With the aid of (4.41), (4.42), and (4.43) and the circuit in Fig. 5, the current-voltage relationships for the source, idler, and pump circuits can be expressed as

$$\tilde{\mathbf{I}}_{\mathbf{s}}(\mathbf{j\omega j} = \left(G_T + j\omega_s a_2 \frac{V_i V_p}{V_s} e^{j\left(\phi_p - \phi_i - \phi_s\right)} \right) \tilde{\mathbf{V}}_{\mathbf{s}}(\mathbf{j\omega j} \tag{4.44}$$

$$0 = \left(G_2 + j\omega_i a_2 \frac{V_s V_p}{V_i} e^{j\left(\phi_p - \phi_i - \phi_s\right)} \right) \tilde{\mathbf{V}}_{\mathbf{i}}(\mathbf{j\omega j} \tag{4.45}$$

$$\tilde{\mathbf{I}}_{\mathbf{p}}(\mathbf{j\omega j} = \left(G_3 + j\omega_p a_2 \frac{V_s V_i}{V_p} e^{-j\left(\phi_p - \phi_i - \phi_s\right)} \right) \tilde{\mathbf{V}}_{\mathbf{p}}(\mathbf{j\omega j}, \tag{4.46}$$

where $G_T = G_s + G_L + G_1$. Applying the resonance conditions of (4.30), (4.31), and (4.32) and substituting (4.45) and (4.46) into (4.44) to eliminate V_i and V_p allows the admittance looking into the source current driver, $\tilde{\mathbf{Y}}_{\mathbf{source}}$, to be expressed in the following manner.

$$\tilde{\mathbf{Y}}_{\mathbf{source}} = G_T - \frac{\omega_s \omega_i a_2^2}{G_2 G_3^2} \frac{|\tilde{\mathbf{I}}_{\mathbf{p}}(\mathbf{j\omega j}|^2}{\left(1 + \frac{\omega_i \omega_p}{G_2 G_3} a_2^2 V_s^2 \right)^2} = G_T - G \tag{4.47}$$

The small-signal transducer gain, g_t, of the circuit in Fig. 5 can now be determined as

$$g_t = \frac{G_L V_s^2}{\frac{|I_s|^2}{4G_s}} = \frac{4G_s G_L}{|\tilde{\mathbf{Y}}_{\mathbf{source}}|^2}. \tag{4.48}$$

By truncating the Taylor series expansion of the charge stored on the plates of the nonlinear capacitor in (4.28), (4.48) will be unable to accurately predict the gain of the amplifier under large-signal operating conditions.

b) Phase-Coherent Degenerate Negative-Resistance Parametric Amplifiers

With degenerate negative-resistance parametric amplifiers, the pump frequency is exactly twice that of the source such that the condition of (4.27) reduces to $f_i = f_s$. Thus, in degenerate mode of operation, there is no need for a separate high-Q resonant trap to contain the idler, reducing the complexity of the circuit model of Fig. 5 to that of Fig. 6.

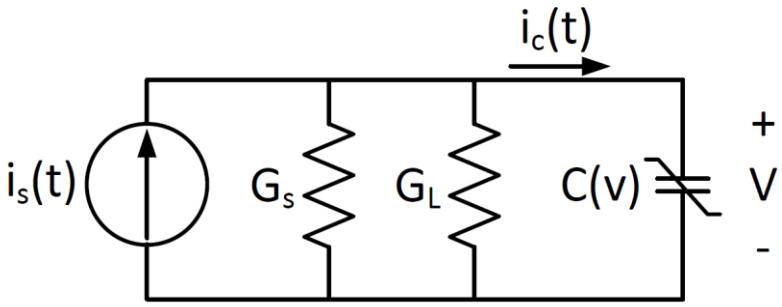

Figure 4.4: An equivalent circuit of a degenerate negative-resistance parametric amplifier. The pump circuit has been omitted, however, its effects have been included in the definition of $C(t)$ in (4.49). The parallel resonant traps have also been omitted by assuming on-resonance operating conditions.

The pump circuit has been omitted from Fig. 6. This is because the nonlinear capacitor's change in capacitance is dominated by the pump voltage swing, therefore the pump circuit can be absorbed into the nonlinear capacitor's model, such that it is now a time-varying capacitance with frequency $\omega_p = 2\omega_s$.

$$C(v_p(t)) = C(t) = 2MC_o \sin\left(2\omega_s t + \phi_p\right), \tag{4.49}$$

where M denotes the coupling between the source and pump voltages, and C_o is the large-signal average capacitance of the nonlinear capacitor. Defining

$$v = V_s \sin\left(\omega_s t + \phi_s\right) \tag{4.50}$$

and substituting (4.49) and (4.50) into the definition of the current passing through a nonlinear capacitor from (4.33), the total current can be expressed as

$$i_c(t) = -\omega_s MC_o V_s \sin\left(\omega_s t + \phi_p - \phi_s\right). \tag{4.51}$$

Applying Kirchoff's Current Law, the source generator current, $i_s(t)$, is

$$i_s(t) = V_s\left(G_s + G_L\right)\sin\left(\omega_s t + \phi_s\right) - \omega_s MC_o V_s \sin\left(\omega_s t + \phi_p - \phi_s\right). \tag{4.52}$$

The small-signal transducer gain, g_t, is then given by

$$g_t = \frac{4G_s G_L V_s^2}{|\tilde{\mathbf{I}}_s \tilde{\mathbf{I}}_s^*|} = \frac{4G_s G_L}{\left(G_s + G_L\right)^2 \underbrace{\left[1 + \beta^2 - 2\beta\cos\left(2\phi_s - \phi_p\right)\right]}_{1}}, \tag{4.53}$$

where

$$\tilde{\mathbf{I}}_{\mathbf{s}} = V_s\left(G_s + G_L\right)e^{j\phi_s} - \omega_s M C_o V_s e^{j\left(\phi_p - \phi_s\right)} \tag{4.54}$$

is the Fourier transform of (4.52), and

$$\beta = \frac{\omega_s M C_o}{G_s + G_L}. \tag{4.55}$$

Equation (4.53) will be unable to predict large-signal gain because of the linear approximation of the change in nonlinear capacitance in (4.49). Term 1 in (4.53) acts to increase the transducer gain and is phase-dependent. This is a consequence of the harmonic relationship between the pump and source frequencies, namely, $\omega_p = 2\omega_s$. The maximum transducer gain occurs when $2\phi_s = \phi_p$ and will then take on the value

$$g_{t,max} = \frac{4G_s G_L}{\left(G_s + G_L\right)^2\left(1-\beta\right)^2}. \tag{4.56}$$

Similar to parametric upconverters, the operating bandwidth of negative-resistance parametric amplifiers will depend on the form of the filtering necessary to isolate the pump, source, and idler currents. Both Figs. 5 and 6 make use of high-Q parallel resonant L-C filters and as a result the bandwidth will be primarily limited by the loaded quality factor of these circuits. Blackwell and Kotzbue approached the problem of the bandwidth of negative-resistance parametric amplifiers by assuming single-tuned resonant structures, and determined that the gain-bandwidth product can be written approximately as

$$g^{1/2}b = \frac{1}{Q_l}, \tag{4.57}$$

where Q_l is the loaded quality factor of the amplifier resonant circuit.

E) Analytical Modeling of Parametric Amplifiers

The theory above focused on the gain and bandwidth of parametric amplifiers from a quasi-idealistic circuit standpoint. Because of the use of quasi-idealistic circuit models used above, the derived expressions offer little aid in the design process of physical parametric systems. By considering more complex, nonidealized circuits, analytical models can be developed that describe power gain, gain-compression, and RF-RF conversion efficiency. These analytical models provide not only a more in-depth understanding of the mechanisms that limit gain, efficiency, and bandwidth of parametric amplifiers, but also contribute a design tool for error correction and optimization of parametric systems.

a) Phase-Incoherent Parametric Upconverting Amplifiers

The derivation performed by Manley and Rowe demonstrated the ideal mathematical

relationship that exists between the mixing products of a nonlinear reactive element under excitation. Their relationships came as a result of the assumptions of incommensurable and periodic excitation signals. Under these two assumptions, it was never necessary for Manley and Rowe to solve the two-dimensional Fourier integrals for the mixing term coefficients. In doing so, and with a proper circuit model for the nonlinear reactance, analytical models can be developed describing the non-ideal achievable gain and efficiency of a parametric upconverter.

Varactor diodes, when operating well below their self-resonance frequency, can be modeled as a series variable resistance, $R_s(v)$, and nonlinear capacitance, $C(v)$, both a function of the varactor's terminal voltage. In the following derivation, it will be assumed that the change in $R_s(v)$ with respect to the terminal voltage is minimal (assuming reverse bias operation) and can be treated as a constant to a first-order approximation. The capacitive change in the varactor can be approximated as a linear function of the terminal voltage, $C(v) = c_0 + c_1 v$, where c_0 is dependent on the bias voltage, and c_1 is some constant of units Farads per volt. In the particular instance of high gain parametric amplifiers, the pump voltage is several orders of magnitude greater than the source, and dominates the terminal voltage such that $C(v)$ can be expressed as a time-varying sinusoidal function with frequency ω_p,

$$C(v) = c_0 + c_1 v|_{v=V_p \cos\omega_p} \approx C_o\left(1 + 2M\cos\omega_p t\right) = C(t), \tag{4.58}$$

where M is proportional to the pump voltage and gives the coupling between the voltages at the two angular frequencies ω_s and ω_p, and C_o is the average large-signal capacitance. Let the charge, q, stored on $C(t)$ be a single-valued function of the terminal voltage $v = V_{DC} + V_s\cos\omega_s t + V_p\cos\omega_p t$. The charge can be expressed as a Taylor series in v to obtain

$$q = q(0) + \frac{\partial q}{\partial v}v + \frac{1}{2}\frac{\partial^2 q}{\partial v^2}v^2 + \cdots, \tag{4.59}$$

where all derivatives are evaluated at $v = V_{DC}$. Since all powers of v exist in (4.59), the frequencies of the charge coefficients will span $\{f_s,\ f_p\}$. Thus, the frequencies of the current coefficients also spans $\{f_s,\ f_p\}$, and the voltage developed across $C(t)$ contains information on all possible mixing products. Consequently, the charge can be represented as a two-dimensional Fourier series,

$$q = \sum_{n=-\infty}^{\infty}\sum_{m=-\infty}^{\infty} q_{n,m} e^{j\left(n\omega_s + m\omega_p\right)t}, \tag{4.60}$$

where the charge series coefficients, $q_{n,m}$, are expressed as

$$q_{n,m} = \frac{1}{4\pi^2}\int_{-\pi}^{\pi}\int_{-\pi}^{\pi}\left(V_{DC} + V_s\cos x + V_p\cos y\right)$$

$$\times C_o\left(1+2M\cos y\right)e^{-j(nx+my)}dxdy, \tag{4.61}$$

with $x=\omega_s t$ and $y=\omega_p t$. The total current, $I_{n,m}$, through $C(t)$ is the total time derivative of the charge series coefficients,

$$I_{n,m}=\frac{dq_{n,m}}{dt}=\frac{\partial q_{n,m}}{\partial t}+\frac{\partial q_{n,m}}{\partial \omega_s}\frac{d\omega_s}{dt}+\frac{\partial q_{n,m}}{\partial \omega_p}\frac{d\omega_p}{dt}. \tag{4.62}$$

However, the initial assumption of the incommensurability of ω_s and ω_p causes $\frac{\partial q_{n,m}}{\partial \omega_s}=\frac{\partial q_{n,m}}{\partial \omega_p}=0$. As a result, (4.62) reduces to the partial time derivative of the charge series terms

$$I=\frac{\partial q}{\partial t}=\sum_{n=-\infty}^{\infty}\sum_{m=-\infty}^{\infty}I_{n,m}e^{j\left(n\omega_s+m\omega_p\right)t} \tag{4.63}$$

$$I_{n,m}=j\left(n\omega_s+m\omega_p\right)q_{n,m}. \tag{4.64}$$

The frequencies of the impedance coefficients $Z_{n,m}$, as with the current coefficients, will span $\{f_s,\ f_p\}$ in the Fourier domain. The representation of $C(t)$ in (4.58), while a good mathematical model for the time-dependent change in capacitance, is a result of large-signal excitation. Thus, (3.1) must be linearized about V_{DC} and can be accurately approximated by C_o to obtain the varactor impedance series terms

$$Z_{n,m}=R_s+\frac{1}{j\left(n\omega_s+m\omega_p\right)C_o}. \tag{4.65}$$

Two-dimensional Fourier synthesis can now be used to express the complex power, P, of the varactor,

$$P=\sum_{n=-\infty}^{\infty}\sum_{m=-\infty}^{\infty}P_{n,m}e^{j\left(n\omega_s+m\omega_p\right)t} \tag{4.66}$$

$$P_{n,m}=\left|I_{n,m}\right|^2 Z_{n,m}. \tag{4.67}$$

Evaluation of (4.67) for the ratio of $P_{1,1}$ to $P_{1,0}$ results in

$$G_o = \frac{P_{1,1}}{P_{1,0}} = \underbrace{\frac{\omega_o}{\omega_s}}_{1} \underbrace{M^2}_{2} \underbrace{\frac{1 + jC_o R_s \omega_o}{1 + jC_o R_s \omega_s}}_{3}. \tag{4.68}$$

We are interested in both the real and reactive power being provided by the varactor, such that (4.68) can be written as $G_o = \Re\{G_o\} + j\Im\{G_o\} = G_r + jG_i$. Separating the real and reactive terms in (4.68) yields

$$G_r = \frac{\omega_o}{\omega_s} M^2 \frac{Q_s}{Q_o} \frac{Q_s Q_o + 1}{Q_s^2 + 1} \tag{4.69}$$

$$G_i = \frac{\omega_o}{\omega_s} M^2 \frac{Q_s}{Q_o} \frac{Q_s - Q_o}{Q_s^2 + 1}, \tag{4.70}$$

where

$$Q_s = \frac{1}{\omega_s R_s C_o} \tag{4.71}$$

$$Q_o = \frac{1}{\omega_o R_s C_o}. \tag{4.72}$$

In (4.58) it was assumed that the varactor's capacitance was piecewise-linear, as in Fig. 7, to describe $C(t)$ as sinusoidal. Making the same assumption, the coupling factor M in term 2 in (4.69) can be treated as a constant and written as a direct function of the change in capacitance experienced under RF excitation at a specified amplitude.

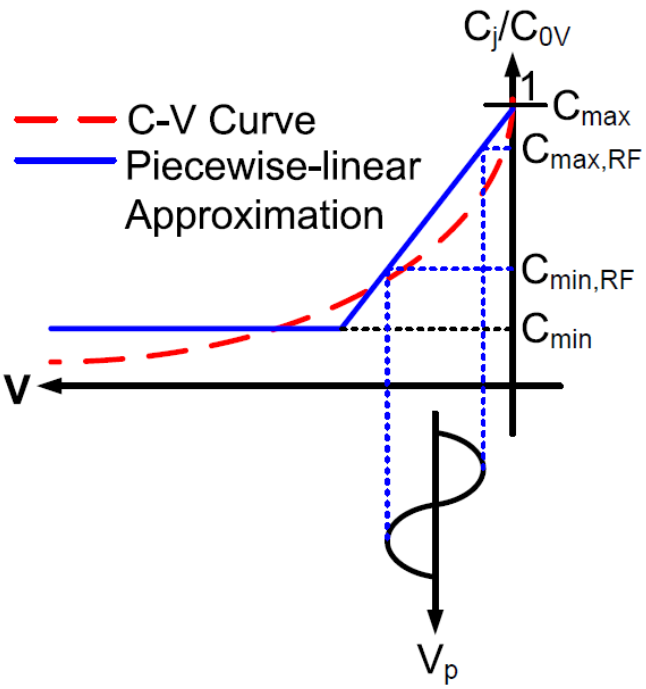

Figure 4.5: Piecewise-linear approximation of the square-law region of the varactor junction capacitance, as normalized to its maximum value at 0V bias, versus ideal characteristics. This figure demonstrates the difference between the varactors maximum available change in capacitance, as opposed to that observed under RF drive.

$$M = \frac{C_{max,RF} - C_{min,RF}}{C_{max,RF}} \qquad M \in (0,1) \tag{4.73}$$

Substitution of (4.73) into (4.71) and (4.72) provides a complete description of the achievable real and reactive gain of a phase-incoherent upconverting parametric amplifier.

$$G_r = \underbrace{\frac{\omega_o}{\omega_s}}_{1}\underbrace{\left(1 - \frac{C_{min,RF}}{C_{max,RF}}\right)^2\left(\frac{Q_s}{Q_o}\frac{Q_s Q_o + 1}{Q_s^2 + 1}\right)}_{2} \tag{4.74}$$

$$G_i = \frac{\omega_o}{\omega_s}\left(1 - \frac{C_{min,RF}}{C_{max,RF}}\right)^2\left(\frac{Q_s}{Q_o}\frac{Q_s - Q_o}{Q_s^2 + 1}\right) \tag{4.75}$$

Manley and Rowe predict the maximum achievable real power gain of any phase-incoherent upconverting parametric amplifier to be $\frac{\omega_o}{\omega_s}$. Therefore, term 2 in (4.75) can

be considered a gain-degradation factor, and

$$\lim_{\substack{\frac{C_{max,RF}}{C_{min,RF}},Q_s,Q_o\to\infty}} G_r = \frac{\omega_o}{\omega_s}, \tag{4.76}$$

as predicted by Manley and Rowe under ideal conditions. Conversely,

$$\lim_{\substack{\frac{C_{max,RF}}{C_{min,RF}}\to 1 \\ \frac{Q_s}{Q_o}\to 0}} G_r = 0. \tag{4.77}$$

For any appreciable value of Q_s and Q_o, the last term in (4.77) is approximately equal to 1. Gain-degradation is therefore dominated by the change in capacitance in the varactor. Let

$$\gamma = \frac{Q_s}{Q_o}\frac{Q_sQ_o+1}{Q_s^2+1} \qquad \gamma \in [0,1]. \tag{4.78}$$

Then, $G_r = f\left(\frac{C_{max,RF}}{C_{min,RF}},\gamma\right)$. Figure 8 shows a family of isolines of the gain-degradation term of (4.77) with $\gamma =$ 0.1, 0.5 and 1.

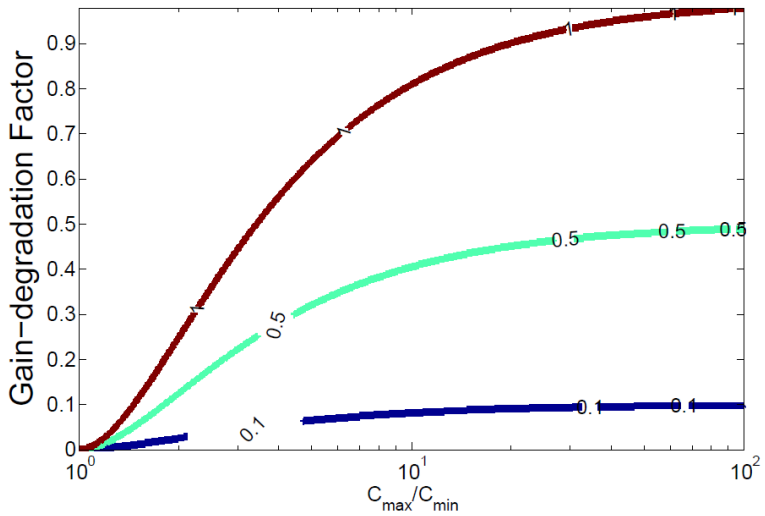

Figure 4.6: Plot of the change in the gain-degradation factor versus varactor capacitance ratio with $\gamma =$ 0.1, 0.5 and 1.

The reactive power gain gives a measure of the mismatch between the varactor and the load. An ideal varactor will deliver all available real power to the load and all reactive power

should be reflected back to the varactor; the reactive gain G_i should be zero. Let

$$\beta = \frac{Q_s}{Q_o}\frac{Q_s - Q_o}{Q_s^2 + 1}. \tag{4.79}$$

Then $G_i = f\left(\frac{C_{max,RF}}{C_{min,RF}}, \beta\right)$. Under ideal conditions, it can be seen that

$$\lim_{\substack{\frac{C_{max,RF}}{C_{min,RF}} \to \infty \\ \beta \to 0}} G_i = 0. \tag{4.80}$$

Equations (4.79) and (4.80) do not include higher order terms that would account for the strong nonlinear effects of gain compression. Therefore, predicting gain-degradation is limited to the linear region of the AM-AM distortion curve and will begin to deviate from measured results as the output power begins to saturate.

The derivation of the achievable efficiency of a phase-incoherent upconverting parametric amplifier proceeds similar to that just performed for the gain and will not be presented with as much detail. There are multiple ways to define system efficiency of phase-incoherent upconverting parametric amplifiers, however one should avoid solving the Manley-Rowe relations for the ratio of the power in the upconverted output to that of the pump, as it results in an equation that predicts an efficiency greater than 100%. The power in the upconverted output must be the sum of the source and pump powers P_s and P_p, respectively, as required by Conservation of Power for a lossless reactance.

$$P_o = P_s + P_p \tag{4.81}$$

For this reason, an accurate way to represent the system efficiency, η, is

$$\eta = \frac{P_o}{P_s + P_p} \tag{4.82}$$

that guarantees the maximum obtainable efficiency under ideal conditions is 100%; this is effectively equivalent to power-added efficiency for transconductance amplifiers. For system efficiency, the power series coefficients given in (4.82) are still valid. In the definition of efficiency presented in (3.25), it can be shown that

$$\eta = \frac{M^2 V_s^2 \omega_o \left(Q_o^{-1} - j\right)}{\left(2MV_{DC} + V_p\right)^2 \omega_p \left(Q_p^{-1} - j\right) + V_s^2 \omega_s \left(Q_s^2 - j\right)}. \tag{4.83}$$

As with gain, both the real and imaginary components of (3.26) are of interest. Equation (4.83) shows the real component of the efficiency, and (3.28) the imaginary component, such that

$\eta = \eta_r + j\eta_i$.

$$\eta_r = \frac{M^2 Q_p Q_s V_s^2 \omega_o \left[\left(1+Q_o Q_p\right) Q_s \left(2MV_{DC}+V_p\right)^2 \omega_p + Q_p \left(1+Q_o Q_s\right) V_s^2 \omega_s \right]}{Q_o \left[\left(1+Q_p^2\right) Q_s^2 \left(2MV_{DC}+V_p\right)^4 \omega_p^2 + 2Q_p Q_s \left(1+Q_p Q_s\right) \left(2MV_{DC}+V_p\right)^2 V_s^2 \omega_p \omega_s + Q_p^2 \left(1+Q_s^2\right) V_s^4 \omega_s^2 \right]} \quad (4.84)$$

$$\eta_i = \frac{M^2 Q_p Q_s V_s^2 \omega_o \left[\left(Q_o - Q_p\right) Q_s \left(2MV_{DC}+V_p\right)^2 \omega_p + Q_p \left(Q_o - Q_s\right) V_s^2 \omega_s \right]}{Q_o \left[\left(1+Q_p^2\right) Q_s^2 \left(2MV_{DC}+V_p\right)^4 \omega_p^2 + 2Q_p Q_s \left(1+Q_p Q_s\right) \left(2MV_{DC}+V_p\right)^2 V_s^2 \omega_p \omega_s + Q_p^2 \left(1+Q_s^2\right) V_s^4 \omega_s^2 \right]} \quad (4.85)$$

Equations (4.84) and (4.85) cannot be simplified in such a way to contain an efficiency-degradation term as was done with the maximum gain. However, functional analysis of (4.84) and (4.85) can be used to confirm the correctness of the derivation. Under ideal conditions, $Q_o, Q_p, Q_s \to \infty$ and $M \to 1$. As a result,

$$\lim_{\substack{M \to 1 \\ Q_{s,p,o} \to \infty}} \eta_r = \frac{V_s^2 \omega_o}{\left(2V_{DC}+V_p\right)^2 \omega_p + V_s^2 \omega_s}. \quad (4.86)$$

In (4.58) it was assumed that $V_p >> V_s$. Consequently, let $V_s = 0$ and equate (34.86) to 1 being the maximum obtainable efficiency. Then,

$$\left(2V_{DC}+V_p\right)^2 \omega_p = 0. \quad (4.87)$$

There is only one solution to the quadratic in (3.30): $V_p = -2V_{DC}$. With reference to Fig. 7, selecting a bias point in the middle of the linear approximation to the square-law region and allowing a symmetric swing in V_p equal to twice the bias voltage ensures that the varactor will experience its available C_{max} to C_{min} ratio. In addition, the terminal voltage of the varactor will exceed its built-in potential, forcing saturated operating conditions. This confirms the derivational necessity of the varactor experiencing its maximum change in terminal capacitance and suggests that driving the phase-incoherent upconverting parametric amplifier into saturation may maximize the efficiency. Conversely,

$$\lim_{\substack{M \to 0 \\ Q_{s,p,o} \to 0}} \eta_r = 0. \quad (4.88)$$

The reactive component of the efficiency provides a measure of the reflective mismatch between the varactor and the load. In the ideal case, the parasitic self-resistance of the varactor goes to zero and the quality factor at all frequencies of operation is infinite.

$$\lim_{Q_{s,p,o}\to\infty} \eta_i = 0 \tag{4.89}$$

It is difficult to determine the dominant terms in (4.86) with uncertainty in its independent variables using a graphical means as was performed with the gain analytical model. Instead, first-order variable sensitivity analysis can be employed to examine the uncertainty of the efficiency analytical model. The first-order sensitivity of a dependent function f with respect to independent variable x is defined as

$$S_x^f = \frac{\partial f}{\partial x}\frac{x}{f}. \tag{4.90}$$

Evaluation of S_x^f at a typical operating point demonstrated the general sensitivity of the efficiency analytical model showing the per unit change in η with a per unit change in Q_o, Q_p, Q_s, and M was insignificant if all are sufficiently large. The sensitivity of η is dominated by the uncertainty in V_s, V_{DC}, and V_p as expected with the choice of initial assumptions. A practical efficiency analytical model is thus described in (4.91).

$$\eta_r \approx \frac{V_s^2 \omega_o}{\left(2V_{DC}+V_p\right)^2 \omega_p + V_s^2 \omega_s} \tag{4.91}$$

Similar to the gain analytical model, the efficiency analytical model is limited to predicting system efficiency in backed-off operating conditions only. Equation (3.34) does not include higher order terms and as a result cannot compensate for saturated operating conditions.

b) Phase-Coherent Degenerate Parametric Amplifiers

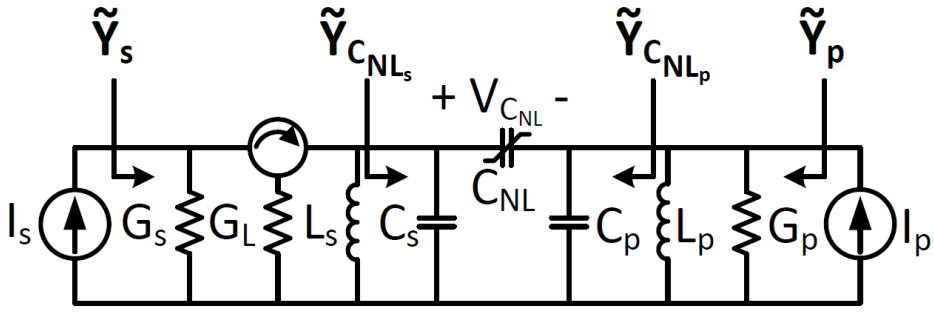

Figure 4.7: A degenerate parametric amplifier utilizing a nonlinear capacitance. The circulator, $L_s - C_s$, and $L_p - C_p$ electrically isolate the output, source, and pump currents, respectively, from one another.

Consider the circuit in Fig. 9 that shows the basic architecture of degenerate parametric

amplifiers. The circuit contains a nonlinear capacitance (NLC) whose junction capacitance is a function of its own terminal voltage, $V_{C_{NL}}$. Source and pump currents are electrically isolated from one another through the high-Q parallel resonant combinations $L_s - C_s$ and $L_p - C_p$ that resonate at ω_s and ω_p, respectively. It is assumed that the circulator's ideal scattering matrix is

$$[S]_{circulator} = \begin{bmatrix} 0 & 0 & 1 \\ 1 & 0 & 0 \\ 0 & 1 & 0 \end{bmatrix} \tag{4.92}$$

for any impedance combination presented to the circulator allowing it to direct incident and reflected waves without affecting their magnitude and phase. This assumption provides for an exploration of the effect of impedance mismatch between only the NLC and G_s, G_p, and G_L in degenerate paramps.

The NLC can be modeled in a Taylor series about some neighborhood of its DC operating point, V_{DC}, as

$$C_{NL}(V) = a + b\left(V_{C_{NL}} - V_{DC}\right), \tag{4.93}$$

where a and b are the Taylor series coefficients with units *F* and *F/V*, respectively. In a degenerate parametric amplifier, voltage potentials at only frequencies ω_s and ω_p need to be present across the terminals of the NLC to generate the negative resistance responsible for power amplification. Therefore, if all unwanted harmonic voltages across the terminals of the NLC are properly shorted,

$$\begin{aligned} v_{C_{NL}}(t) = {} & \frac{V_p}{2}\left(e^{j\left(2\omega_s t + \phi_p - \frac{\pi}{2}\right)} + e^{-j\left(2\omega_s t + \phi_p - \frac{\pi}{2}\right)} \right) \\ & + \frac{V_s}{2}\left(e^{j\left(\omega_s t + \phi_s - \frac{\pi}{2}\right)} + e^{-j\left(\omega_s t + \phi_s - \frac{\pi}{2}\right)} \right), \end{aligned} \tag{4.94}$$

where V_s and V_p are the peak amplitude values of the voltage waveforms at ω_s and ω_p, respectively, across the terminals of the NLC. It is necessary to consider an initial phase displacement of 90 degrees lagging in (4.94) if the NLC is to properly present a negative resistance. The time-varying currents through a NLC can be determined from the time-varying voltage applied to its terminals by

$$i_{C_{NL}}(t) = C_{NL}\left(v_{C_{NL}}(t)\right)\frac{\partial v_{C_{NL}}(t)}{\partial t}. \tag{4.95}$$

By substituting (4.93) and (4.94) into (4.95) and expanding, collecting terms at ω_s and ω_p, bringing the solution over to the positive frequency spectrum, and dividing the terms at ω_s by $V_s e^{j\omega_s t+\phi_s}$ and the terms at ω_p by $V_p e^{2j\omega_s t+\phi_p}$, equivalent admittances for the NLC are obtained at both ω_s and ω_p.

$$\tilde{\mathbf{Y}}_{\mathbf{C_{NL_s}}} = \omega_s\left(ja - \frac{be^{j\left(\phi_p-2\phi_s\right)}V_p}{2}\right) \tag{4.96}$$

$$\tilde{\mathbf{Y}}_{\mathbf{C_{NL_p}}} = \omega_s\left(2ja + \frac{be^{j\left(2\phi_s-\phi_p\right)}V_s^2}{2V_p}\right) \tag{4.97}$$

Using (4.96) and (4.97), and applying Euler's formula to each complex exponential, the total admittance seen by the source and pump generators, $\tilde{\mathbf{Y}}_{\mathbf{s}}$ and $\tilde{\mathbf{Y}}_{\mathbf{p}}$, can be expressed as

$$\begin{aligned}\tilde{\mathbf{Y}}_{\mathbf{s}} &= G_s - \frac{\omega_s b V_p}{2}\cos\left(\phi_p - 2\phi_s\right) \\ &\quad + j\left(\frac{\omega_s b V_p}{2}\sin\left(\phi_p - 2\phi_s\right) + \omega_s a\right)\end{aligned} \tag{4.98}$$

$$\begin{aligned}\tilde{\mathbf{Y}}_{\mathbf{p}} &= G_p + \frac{\omega_s b V_s^2}{2V_p}\cos\left(2\phi_s - \phi_p\right) \\ &\quad + j\left(\frac{\omega_s b V_s^2}{2V_p}\sin\left(2\phi_s - \phi_p\right) + 2\omega_s a\right).\end{aligned} \tag{4.99}$$

Equations (4.98) and (4.99) reveal that the phase relationship $\phi_p = 2\phi_s$ must exist if both the negative conductance is to be maximized and the excess nonlinear reactance (which results from pumping the NLC) is to be minimized.

To ensure that the phase condition stated above is satisfied, the linear susceptance terms $j\omega_s a$ and $2j\omega_s a$ in $\tilde{\mathbf{Y}}_{\mathbf{s}}$ and $\tilde{\mathbf{Y}}_{\mathbf{p}}$, respectively, must be properly eliminated through resonance. This can be accomplished if the values for L_s and L_p in Fig. 9 fulfill

$$L_s = \frac{1}{\omega_s^2\left(C_s + a\right)},\ and\ L_p = \frac{1}{4\omega_s^2\left(C_p + 2a\right)}. \tag{4.100}$$

Then, (4.99) and (4.100) can be substituted into the other such that each is now a function of its own peak terminal voltage V_s or V_p.

$$\tilde{\mathbf{Y}}_{\mathbf{s}} = G_s - \frac{\omega_s b I_p}{2G_p} + \frac{(\omega_s b V_s)^2}{4G_p} \tag{4.101}$$

$$\tilde{\mathbf{Y}}_{\mathbf{p}} = G_p + \frac{2bI_s^2}{V_p(\omega_s b V_p - 2G_s)^2} \tag{4.102}$$

Equations (4.101) and (4.102) show that the circuit in Fig. 9 can be modeled as two separate equivalent circuits from the viewpoints of the source current generator and the pump current generator.

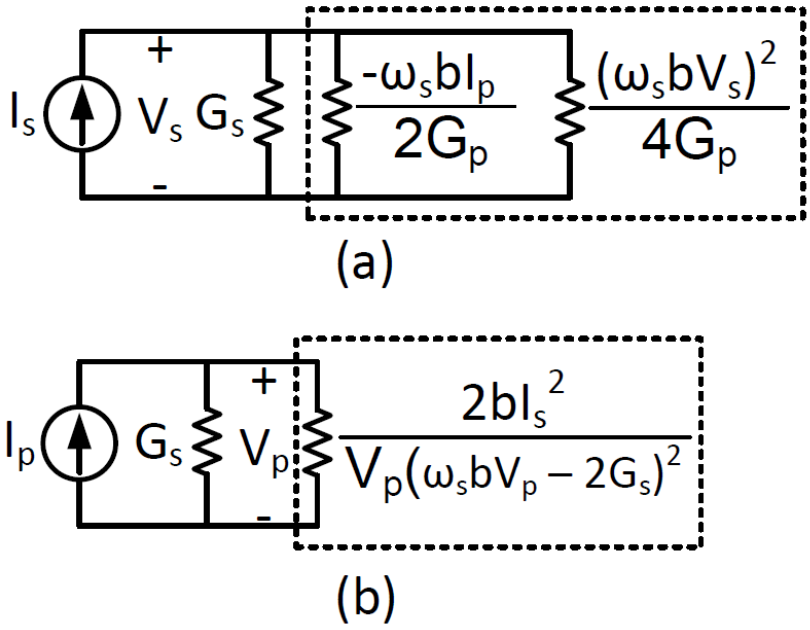

Figure 4.8: Equivalent circuits of the degenerate parametric amplifier in Fig. 9 as seen by (a) the source current generator, and (b) the pump current generator.

Now, from (4.102) and Fig. 10, an expression for the transducer gain, g_t, can be derived.

$$g_t(P_L) = \frac{8G_s\left(\underbrace{\frac{\omega_s b I_p}{2G_p}}_{1} - \underbrace{\frac{(\omega_s b)^2}{2G_L G_p}}_{2} P_L\right)^2}{G_L\left(G_s - \underbrace{\frac{\omega_s b I_p}{2G_p}}_{3} + \underbrace{\frac{(\omega_s b)^2}{2G_L G_p}}_{4} P_L\right)^2} \tag{4.103}$$

Equation (4.103) reveals the mechanism of gain compression in phase-coherent degenerate parametric amplifiers. If the available source power level, $P_{s,av} = \frac{I_s^2}{8G_s}$, is increased, and all other variables in (4.103) remain constant, then terms 2 and 4 increase in magnitude and eventually become comparable in magnitude to terms 1 and 3. This results in a nonlinear decrease in the power delivered to the load causing amplitude modulation distortion of the output. When considering backoff operating conditions, terms 2 and 4 in (4.103) can be ignored and the linear transducer gain, $g_{t,lin}$, can be determined to be

$$g_{t,lin} = \frac{2G_s\left(\omega_s b I_p\right)^2}{G_L G_p^2\left(G_s - \frac{\omega_s b I_p}{2G_p}\right)^2}. \tag{4.104}$$

The RF-RF conversion efficiency of phase-coherent degenerate parametric amplifiers can also be explored. Consider the expression for the total admittance seen by the pump current generator, $\tilde{\mathbf{Y}}_\mathbf{p}$, in (4.104). By applying the phase condition $\phi_p = 2\phi_s$, $\tilde{\mathbf{Y}}_\mathbf{p}$ can be simplified to a useful expression involving both the source and pump voltage amplitudes V_s and V_p.

$$\tilde{\mathbf{Y}}_\mathbf{p} = G_p + \frac{\omega_s b V_s^2}{2V_p G_s} \tag{4.105}$$

This new expression for $\tilde{\mathbf{Y}}_\mathbf{p}$ provides an equivalent circuit from the perspective of the pump current generator, as seen in Fig. 4.9.

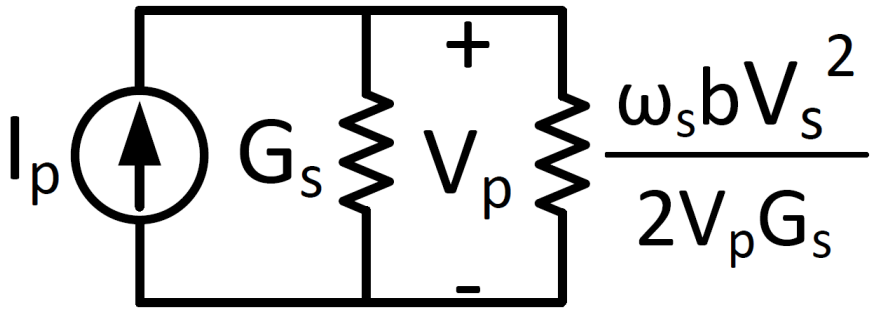

Figure 4.9: Equivalent circuit as seen by the pump current generator according to (4.105).

If it is assumed that G_p is close in value to $\frac{\omega_s b V_s^2}{2V_p G_s}$ then the peak voltage V_p can be

approximated as

$$V_p = \frac{I_p}{2G_p}. \tag{4.106}$$

From (3.48) and (3.49), the available pump power can be expressed as

$$P_{p,av} = \frac{I_p \omega_s b P_L}{8 G_p G_L}, \tag{4.107}$$

where $P_L = \left(\frac{V_s}{\sqrt{2}} \right)^2 G_L$. By defining the RF-RF conversion efficiency as the ratio of output power to available pump power, the efficiency of negative-resistance parametric amplifiers can be expressed as

$$\eta = \frac{P_L}{P_{p,av}} = \frac{8 G_p G_L}{I_p \omega_s b}. \tag{4.108}$$

c) Phase-Coherent Upconverting Parametric Amplifiers

Phase-coherent upconverting parametric amplifiers combine traits from both phase-incoherent upconverting parametric amplifiers and phase-coherent negative-resistance parametric amplifiers. With phase-coherent upconverting parametric amplifiers, the source and pump frequencies are commensurate (as with degenerate parametric amplifiers), but the output is taken at a harmonic (greater than the first) of the source frequency. In this way, phase-coherent upconverting parametric amplifiers mix the source input up to a higher harmonic with gain through the action of a negative resistance.

In the development of the Manley-Rowe relations, the authors explicitly maintained the incommensurability of the two mixing frequencies f_1 and f_2. The validity of the Manley-Rowe relations when dealing with commensurate frequencies f_1 and f_2 was investigated and concluded that they are still valid when the two frequencies are commensurate, however, the two signals must maintain phase incoherence. The imposition of phase incoherence in no way restricts a new mathematical exploration of the possibility of a phase-coherent upconverting parametric amplifier.

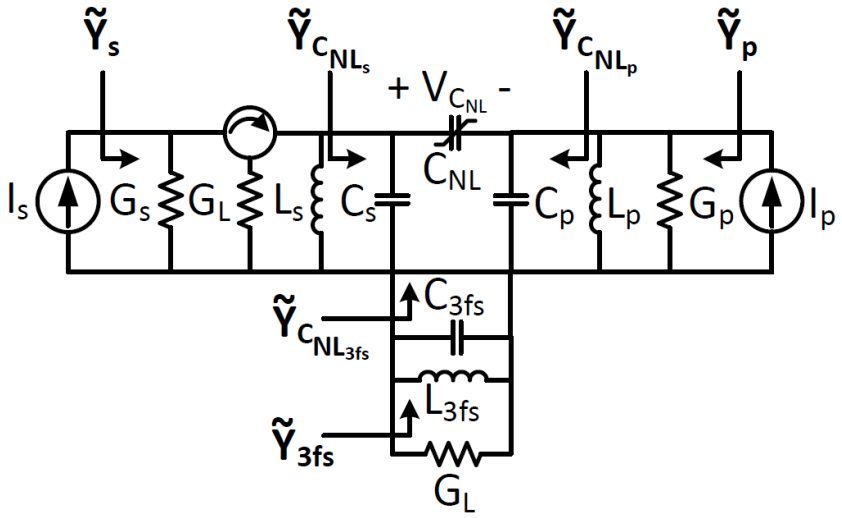

Figure 4.10: Idealized equivalent circuit for a phase-coherent upconverting parametric amplifier utilizing a nonlinear capacitance. The circulator, $L_s - C_s$, $L_p - C_p$, and $L_{3fs} - C_{3fs}$ electrically isolate the source, pump, and output currents, respectively, from one another.

Consider the circuit in Fig. 12 that shows the basic architecture of a phase-coherent upconverting parametric amplifier designed to upconvert to three times the source frequency when $\omega_p = 2\omega_s$. The circuit contains a nonlinear capacitor whose capacitance is a function of its own terminal voltage, $V_{C_{NL}}$. Source, pump, and upconverted output currents are electrically isolated from one another through the high-Q parallel resonant combinations $L_s - C_s$, $L_p - C_p$, and $L_{3fs} - C_{3fs}$ that resonate at ω_s, ω_p, and ω_{3fs}, respectively. It is assumed that the circulator's ideal scattering matrix is

$$[S]_{circulator} = \begin{bmatrix} 0 & 0 & 1 \\ 1 & 0 & 0 \\ 0 & 1 & 0 \end{bmatrix} \tag{4.109}$$

for any impedance combination presented to the circulator allowing it to direct incident and reflected waves without affecting their magnitude and phase. This assumption provides for an exploration of the effect of impedance mismatch between only the NLC and G_s, G_p, and G_L in phase-coherent upconverting parametric amplifiers.

The NLC can be modeled in a Taylor series about some neighborhood of its DC operating point, V_{DC}, as

$$C_{NL}(V) = a + b\left(V_{C_{NL}} - V_{DC}\right), \tag{4.110}$$

where a and b are the Taylor series coefficients with units *F* and *F/V*, respectively. In a phase-coherent upconverting parametric amplifier, voltage potentials at only frequencies ω_s,

ω_p, and ω_{3fs} need to be present across the terminals of the NLC to generate the negative resistance responsible for power amplification at the third harmonic. Therefore, if all unwanted harmonic voltages across the terminals of the NLC are properly shorted,

$$v_{C_{NL}}(t) = \frac{V_p}{2}\left(e^{j\left(2\omega_s t+\phi_p-\frac{\pi}{2}\right)}+e^{-j\left(2\omega_s t+\phi_p-\frac{\pi}{2}\right)}\right) + \frac{V_s}{2}\left(e^{j\left(\omega_s t+\phi_s-\frac{\pi}{2}\right)}+e^{-j\left(\omega_s t+\phi_s-\frac{\pi}{2}\right)}\right) + \frac{V_{3fs}}{2}\left(e^{j\left(3\omega_s t+\phi_{3fs}-\frac{\pi}{2}\right)}+e^{-j\left(3\omega_s t+\phi_{3fs}-\frac{\pi}{2}\right)}\right), \quad (4.111)$$

where V_s, V_p, and V_{3fs} are the peak amplitude values of the voltage waveforms at ω_s, ω_p, and ω_{3fs}, respectively, across the terminals of the NLC. It is necessary to consider an initial phase displacement of 90 degrees lagging in (4.111) if the NLC is to properly present a negative resistance. The time-varying currents through a NLC can be determined from the time-varying voltage applied to its terminals by

$$i_{C_{NL}}(t) = C_{NL}\left(v_{C_{NL}}(t)\right)\frac{\partial v_{C_{NL}}(t)}{\partial t}. \quad (4.112)$$

By substituting (4.110) and (4.111) into (4.112) and expanding, collecting terms at ω_s, ω_p, and ω_{3fs}, bringing the solution over to the positive frequency spectrum, and dividing the terms at ω_s by $V_s e^{j\omega_s t+\phi_s}$, the terms at ω_p by $V_p e^{2j\omega_s t+\phi_p}$, and the terms at ω_{3fs} by $V_{3fs}e^{3j\omega_s t+\phi_{3fs}}$, equivalent admittances for the NLC are obtained at ω_s, ω_p, and ω_{3fs}.

$$\tilde{\mathbf{Y}}_{\mathbf{C_{NL_s}}} = \omega_s\left[ja-\frac{bV_p}{2}\left(e^{j\left(\phi_p-2\phi_s\right)}+e^{j\left(\phi_{3fs}-\phi_p-\phi_s\right)}\frac{V_{3fs}}{V_s}\right)\right] \quad (4.113)$$

$$\tilde{\mathbf{Y}}_{\mathbf{C_{NL_p}}} = \omega_s\left[2ja+\frac{bV_s}{2V_p}\left(e^{j\left(2\phi_s-\phi_p\right)}V_s-2e^{j\left(\phi_{3fs}-\phi_p-\phi_s\right)}V_{3fs}\right)\right] \quad (4.114)$$

$$\tilde{\mathbf{Y}}_{\mathbf{C_{NL_{3fs}}}} = \omega_s\left[3ja+\frac{3bV_sV_pe^{j\left(\phi_s+\phi_p-\phi_{3fs}\right)}}{2V_{3fs}}\right] \quad (4.115)$$

Using (4.113), (4.114), and (4.115), imposing the phase relationships $\phi_p = 2\phi_s$ and $\phi_{3fs} = 3\phi_s$,

and selecting the resonance combinations $L_s - C_s$, $L_p - C_p$, and $L_{3fs} - C_{3fs}$ such that

$$L_s = \frac{1}{\omega_s^2 (C_s + a)} \tag{4.116}$$

$$L_p = \frac{1}{4\omega_s^2 (C_p + 2a)} \tag{4.117}$$

$$L_{3fs} = \frac{1}{9\omega_s^2 (C_{3fs} + 3a)}, \tag{4.118}$$

to eliminate the linear suscptance terms $j\omega_s a$, $2j\omega_s a$, and $3j\omega_s a$ from (4.117), (4.117), and (4.118), respectively, the total admittance seen by the source and pump generators, $\tilde{\mathbf{Y}}_\mathbf{s}$, $\tilde{\mathbf{Y}}_\mathbf{p}$, and $\tilde{\mathbf{Y}}_\mathbf{3fs}$ can be expressed as

$$\tilde{\mathbf{Y}}_\mathbf{s} = G_s - \frac{\omega_s b V_p}{2}\left(1 + \frac{V_{3fs}}{V_s}\right) \tag{4.119}$$

$$\tilde{\mathbf{Y}}_\mathbf{p} = G_p + \underbrace{\frac{\omega_s b V_s}{2V_p}\left(V_s - 2V_{3fs}\right)}_{1} \tag{4.120}$$

$$\tilde{\mathbf{Y}}_\mathbf{3fs} = \frac{3\omega_s b V_s V_p}{2V_{3fs}}. \tag{4.121}$$

Assuming that term 1 in (4.119) is matched to G_p, V_p can be approximated as $V_p = \frac{I_p}{2G_p}$. Using (3.62) and the approximation of V_p to eliminate V_s and V_p from (4.121), the peak current passing through the nonlinear capacitor in Fig. 12 at the third harmonic is

$$I_{3fs} = \frac{3\omega_s b I_p \left(4G_p I_s + \omega_s b I_p V_{3fs}\right)}{16 G_p^2 G_s}. \tag{4.122}$$

From (3.65), it can then be shown that the transducer gain, g_t, from ω_s to $3\omega_s$ is

$$g_t(V_L) = \frac{288\left(\omega_s b I_p\right)^2 G_s G_p G_L \left(2G_p I_s + \omega_s b I_p V_L\right)}{I_s \underbrace{\left[256\left(G_s G_L G_p^2\right)^2 - 9\left(\omega_s b I_p\right)^4\right]}_{1}}. \tag{4.123}$$

It is clear from (3.66) that the parameters G_s, G_p, and G_L may be selected to provide any amount of gain for a given NLC.

The RF-RF conversion efficiency of phase-coherent upconverting parametric amplifiers can also be explored using (3.65) when defining conversion efficiency as the ratio of output power at ω_{3fs} to the available pump power at ω_p.

$$\eta = \frac{288\left(\omega_s b G_p\right)^2 I_s G_L \left(2G_p I_s + \omega_s b I_p V_L\right)}{256\left(G_s G_L G_p^2\right)^2 - 9\left(\omega_s b I_p\right)^4} \tag{4.124}$$

F) Design and Performance of Upconverting and Negative-Resistance Parametric Amplifiers

The analytical models derived above provide a set of design equations for developing parametric upconverters and negative-resistance parametric amplifiers. However, by themselves, the analytical models are not sufficient to construct an entire parametric system. The parametric amplifier must be embedded in an architecture that not only supports the necessary conditions outlined in previous chapters for achieving high gain and broad bandwidth, but must also provide isolation between the source, pump, and/or output/idler circuits, and properly transform impedances to their optimal values.

a) VHF and RF Phase-Incoherent Upconverting Parametric Amplifiers

Two phase-incoherent upconverting parametric amplifiers were constructed. Both upconverting amplifiers were similarly designed following the topology of Fig. 13. The first amplifier upconverted a 30 MHz signal to 300 MHz through parametric mixing with a 270 MHz pump. Varactor diodes were used to act at the nonlinear capacitive mechanism. The varactor diode chosen was the 1S2208 (characteristically similar to the BB833) that has a junction capacitance range of approximately 5 pF at maximum reverse bias to 50 pF at zero bias with a minimum quality factor of 130 at 50 MHz. The varactors were placed in anti-parallel such that the upconverted output currents were in anti-phase to create a virtual ground between the two varactors at the upconverted frequency. This balanced operation allowed for the pump and source circuits to be introduced at the virtual ground without shorting the upconverted output current. Electrical isolation between the pump and source was accomplished using high-Q resonant traps that also assisted in transforming the varactor impedance to its optimal value at the pump and source frequencies. The balanced upconverted currents were then combined using a coaxial balun that also acted as the output match to transform a standard 50 Ohm load to 100 Ohms differential. The DC bias voltages were introduced through transmission lines a quarter-wavelength long at the upconverted output frequency and connected to the balun's balanced inputs. These transmission lines prevented leakage currents at the upconverted frequency.

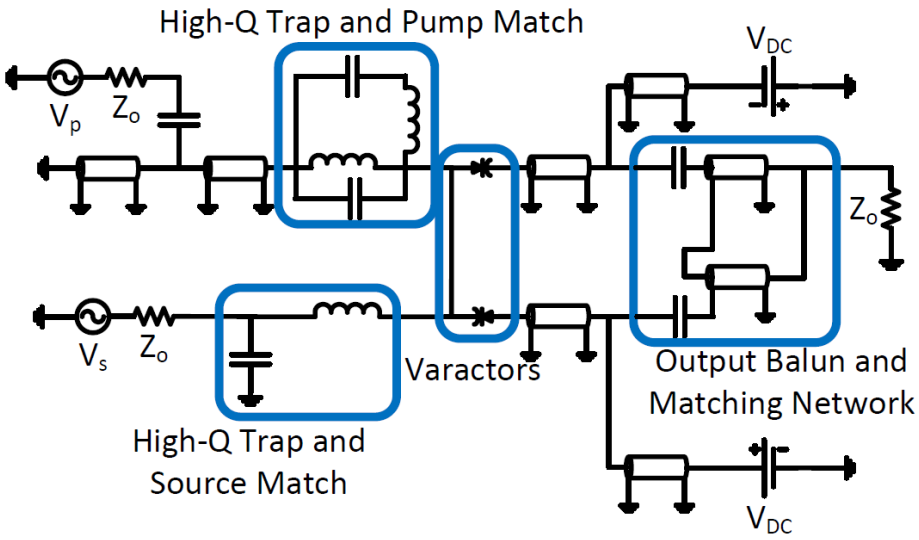

Figure 4.11: Circuit topology for both the VHF and RF phase-incoherent upconverting parametric amplifiers.

The VHF upconverting parametric amplifier was first simulated in a harmonic-balance simulator using standard SPICE models for all components. Simulations predicted a linear power gain of approximately 8 dB at a pump power level of 20 dBm when practical losses were included in all circuit components. Using the definition of efficiency in (3.25), a maximum RF-RF conversion efficiency of 50.7% was achieved in saturated conditions. Simulations estimated the 3 dB bandwidth to be approximately 29.48 MHz to 31.2 MHz, or 4.73% fractional bandwidth.

The breadboard shown in Fig. 14 was fabricated to compare measured performance to simulated results.

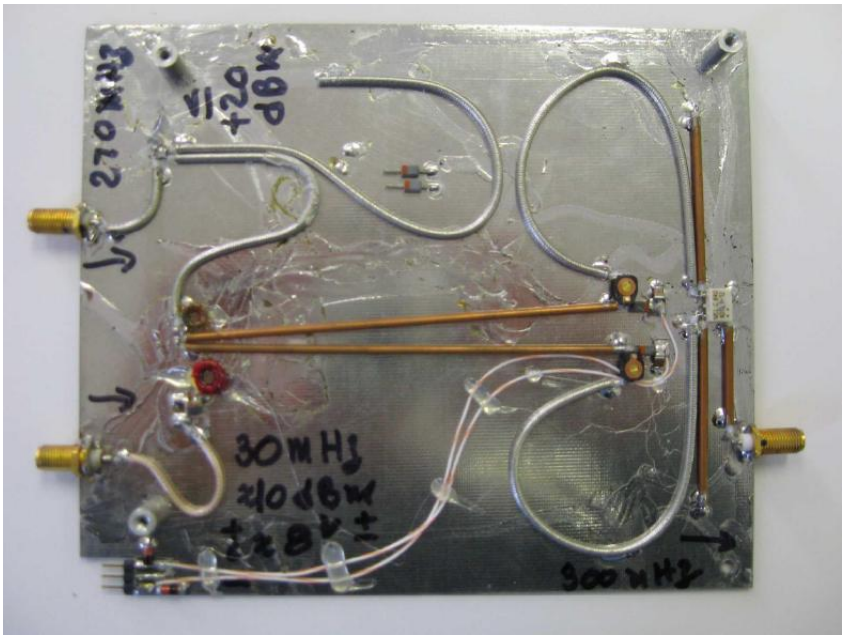

Figure 4.12: Hardware implementation of the VHF upconverting parametric amplifier.

By increasing the source power level, the 1-dB compression point was measured to be 16.87 dBm at $P_s = 10.86$ dBm and $P_p = 20$ dBm. This translated to an efficiency in saturated conditions of 48.6%. At that signal drive level, the varactor became forward biased and created a hard saturation where the output power remained at 16.87 dBm regardless of any increase in P_s. As a result, P_{3dB} was also measured to be approximately 16.87 dBm. The 3-dB bandwidth was next determined. Because of the tuned circuits on the source, pump, and output side, the 3-dB bandwidth is narrow and was measured to be 28.28 MHz to 31.3 MHz, or a 10.1% bandwidth. Figure 15 shows the agreement between simulated and breadboard measurements for gain compression and efficiency at the optimal pump power level and DC bias point.

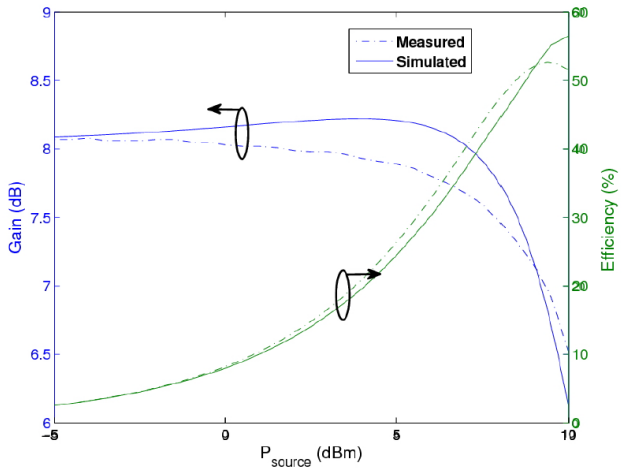

Figure 4.12: Simulated and measured gain and efficiency versus source power for the VHF upconverting parametric amplifier.

The analytical model in (4.117) predicts that the parametric amplifier will maximize its gain when the change in varactor junction capacitance is at its maximum. Care must be taken to limit the voltage swing across the varactor's terminals to prevent the diode from entering forward conduction. The differential design and optimal bias point establish a voltage swing across the varactor causing a capacitive change from 7.40 pF to 49.95 pF at $P_p = 20$ dBm. This results in a maximum-to-minimum capacitance ratio of 6.74. The quality factor of the varactor at the source, pump, and upconverted frequencies can be found by derating the varactor quality factor from 130 as measured at 50 MHz, however, γ in (3.21) will approximately be 1 since the quality factor is high for these frequencies. Therefore, gain degradation will be dominated by the experienced change in varactor capacitance under large-signal excitation. Application of (3.17) under optimal bias conditions and pump drive power results in

$$G_o = \frac{300MHz}{30MHz}\left(1-\frac{7.4pF}{49.95pF}\right)^2 = 8.61dB. \qquad (4.125)$$

The maximum measured gain at $P_p = 20$ dBm and optimal bias point, $V_{bias} = -9$ V, is 8.16 dB. Thus, the discrepancy between measured and calculated gain is 0.45 dB. The use of a piecewise-linear model for the reactive nonlinearity accounts for the small error between measured and calculated power gain.

The analytical model is not limited to predicting gain degradation under optimal operating conditions; it can also predict the change in gain as the capacitance ratio deviates from its maximum. Reducing the pump input power decreases the voltage swing across the varactor and limits the achievable capacitive ratio. At $P_p = 15$ dBm, the varactor junction capacitance changes from 11.1 pF to 49.95 pF resulting in a capacitance ratio of 4.4. Equation (3.17) then predicts a maximum power gain of

$$G_o = \frac{300MHz}{30MHz}\left(1-\frac{11.1pF}{49.95pF}\right)^2 = 7.82dB. \qquad (4.126)$$

Breadboard measurements under identical non-optimal conditions show a maximum obtainable power gain of 7.71 dB, which is a 0.11 dB discrepancy from the analytical model prediction.

The VHF parametric upconverter was then tested over a broad range of operating conditions and the measured data was compared to values predicted by (4.117) and (4.127). Figure 16 compares measured and predicted values for the linear gain against changing pump and source power levels for a constant bias voltage, and Fig. 17 compares measured and predicted values for the linear efficiency against changing bias levels and source power levels at a constant pump power level.

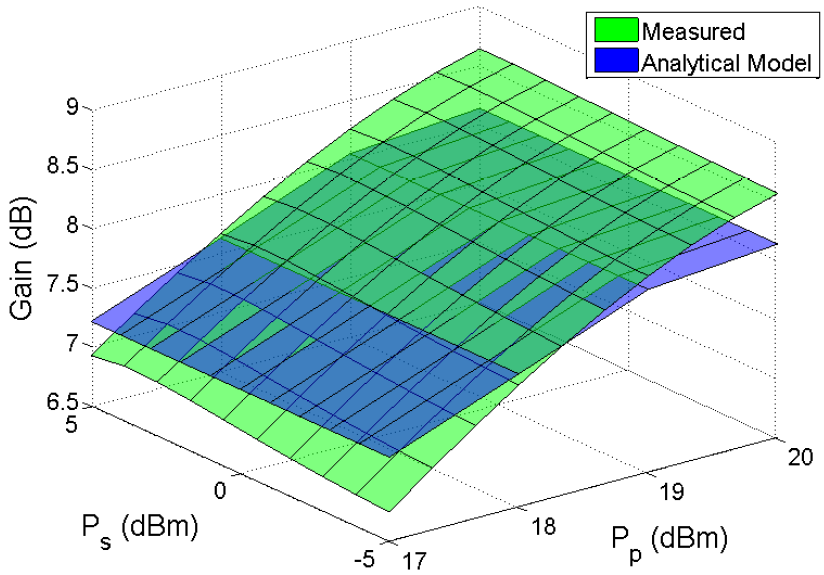

Figure 4.13: Comparison of surface plots of the measured gain of the VHF breadboard upconverting parametric amplifier against predicted by the analytical model of (4.117).

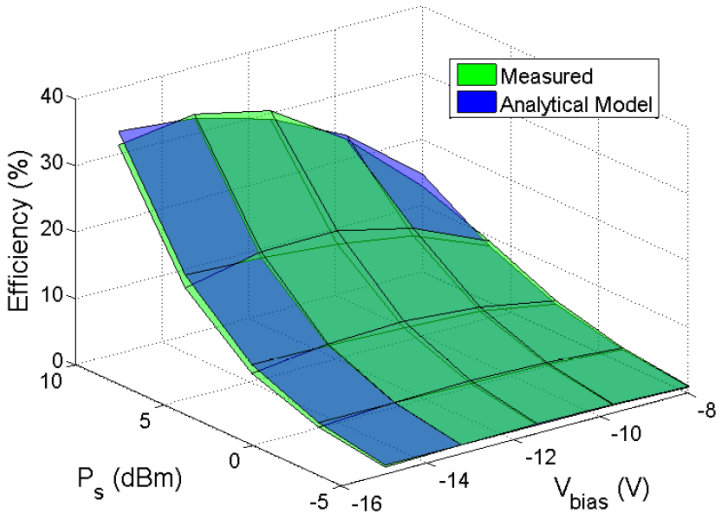

Figure 4.14: Comparison of surface plots of the measured system efficiency of the VHF breadboard upconverting parametric amplifier against predicted by the analytical model of (4.134).

The small error between the analytical prediction and measured response can be graphically explained. Consider a small perturbation in the terminal voltage of the varactor about an operating point near the breakpoint of the piecewise-linear C-V curve, as seen in Fig. 18(a). The resulting change in capacitance is greater for the piecewise-linear curve than that of the actual since the slope of the actual curve is less than that of the approximation near the operating point. As a result, the gain analytical model overestimates the change in capacitance and returns a value greater than is measured. Conversely, in Fig. 18(b), the perturbation is applied about a bias point near zero volts where the slope of the actual C-V curve is greater than the slope of the piecewise-linear. The gain analytical model now underestimates the change in capacitance and returns a value that is less than measured. This error could be corrected by implementing a more complex model for the C-V curve of the varactor but the resulting equation is much more complex and is of little practical use for the purposes of circuit design.

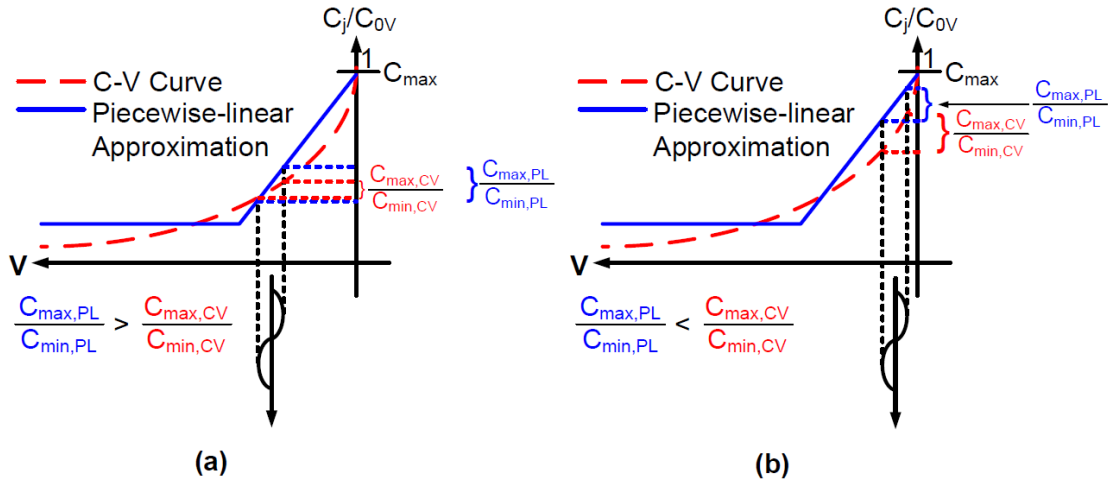

Figure 15: Mathematical reasoning behind the error between the prediction made by the gain analytical model of (3.17) and the measured results from the VHF breadboard upconverting parametric amplifier.

The second upconverting parametric amplifier translated a 140 MHz input to 1.3 GHz through parametric mixing with a 1.16 GHz pump source. As with the previously discussed upconverting parametric amplifier, the 1S2208 varactor diode was chosen as the nonlinear capacitor for it's high quality factor and available change in capacitance. The design of this RF upconverter was practically identical to the previously discussed following an architecture and layout similar to Fig. 13.

The RF upconverting parametric amplifier was first modeled in a harmonic balance simulator using standard SPICE models for all circuit components. Simulations predicted a linear power gain of 4 dB and a maximum efficiency of 30% in backoff at $P_p = 23$ dBm when practical losses were included in the transmission lines. Once constructed, the RF upconverting parametric amplifier demonstrated a maximum gain and efficiency of 4.5 dB and 37%, respectively, as P_s approached saturated operating levels.

The performance of the RF upconverting parametric amplifier and the ability of the analytical models in (3.17) and (3.27) to accurately predict the gain and efficiency across a wide range of operating points can be determined from the constructed breadboard. To compute the predicted responses from the gain and efficiency analytical models, the varactor terminal voltage swing must be known at both the pump and source frequencies. Simulated measurements were used to determine both the capacitance ratio of the varactor under excitation and the peak source voltage at the varactor terminals. Because of the accuracy of the simulated results as compared to the measured results from the breadboard parametric upconverter, the simulated capacitance ratio and peak source voltage at the varactor terminals are considered to be indicative of what would be physically measured on the breadboard upconverting parametric amplifier.

Figure 19 compares the surface plot of the measured gain of the breadboard upconverting parametric amplifier to that predicted by the analytical model of (3.17), and Fig. 20 compares the measured efficiency to that predicted by the analytical model of (3.27). The small error between the measured and predicted values for both figures can be explained using

the same argument presented above for the VHF upconverting parametric amplifier.

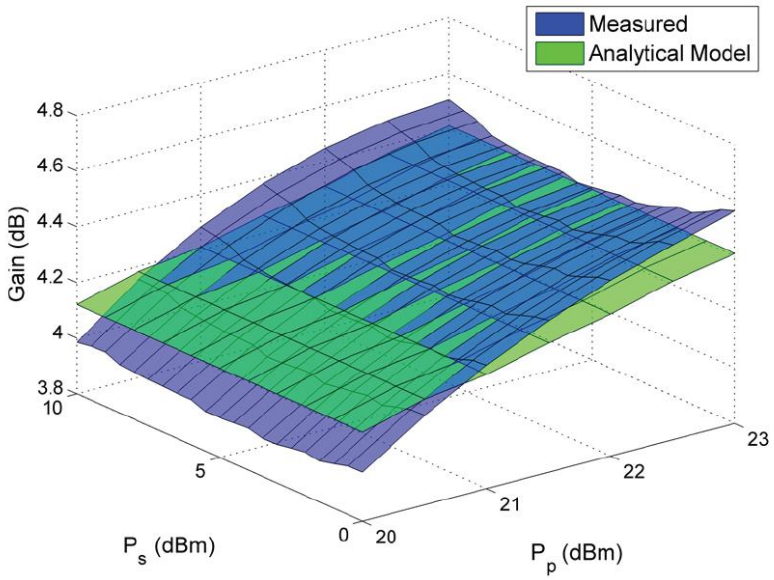

Figure 4.16: Surface plot comparison of the measured gain of the RF breadboard upconverting parametric amplifier to that predicted by the analytical model of (4.117).

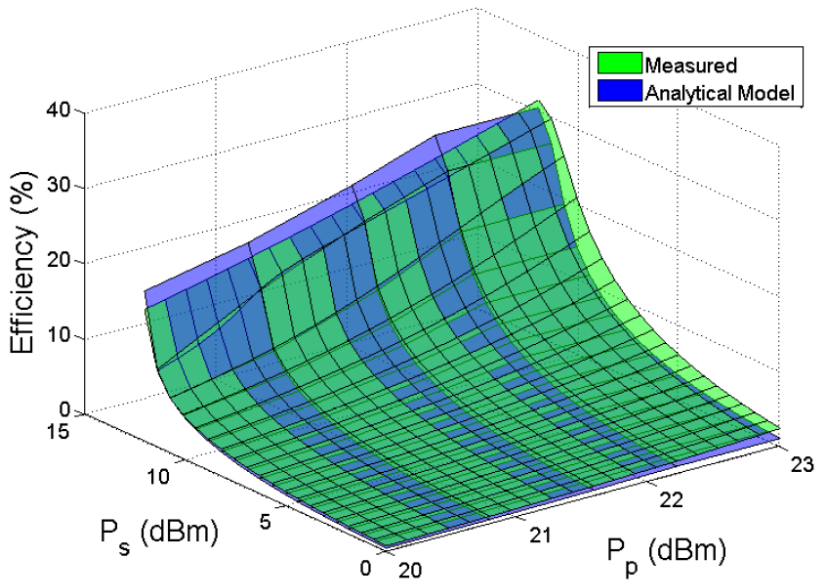

Figure 4.17: Comparison of surface plots of the measured system efficiency of the breadboard parametric upconverter against the predicted efficiency of the analytical model of (4.134).

b) Phase Coherent Negative-Resistance Degenerate Parametric Amplifiers

Three fundamental conditions must be satisfied for a nonlinear capacitance to exhibit a negative resistance. First, a large-signal pumping source is needed to drive the nonlinear action. Second, the large-signal average capacitance of the nonlinear capacitor, C_o, must be eliminated by an attached resonant network, and, finally, the resonant network must properly isolate currents at ω_s from those at ω_p. It was demonstrated above that when these three requirements are satisfied, and the resonant conditions

$$L_s = \frac{1}{\omega_s^2 (C_s + C_o)} \; and \; L_p = \frac{1}{\omega_p^2 (C_p + C_o)} \tag{4.127}$$

are established, (4.127) will predict the small-signal transducer gain, g_t, of a degenerate negative-resistance parametric amplifier.

To satisfy the three fundamental conditions outlined above across a broad range of operating frequencies, a double-balanced mixer (DBM) architecture was adopted. Double-balanced structures have the advantage of inherent isolation at all ports, broadband rejection of pump noise, spurious signals, and intermodulation products, and broadband operation. Conversely, the primary disadvantages of double-balanced mixer architectures are that they require four diodes and two baluns. However, the advantages of a double-balanced mixer architecture outweigh the disadvantages, making it ideal for use as a degenerate parametric amplifier architecture. Figure 4.18 shows a double-balanced ring mixer.

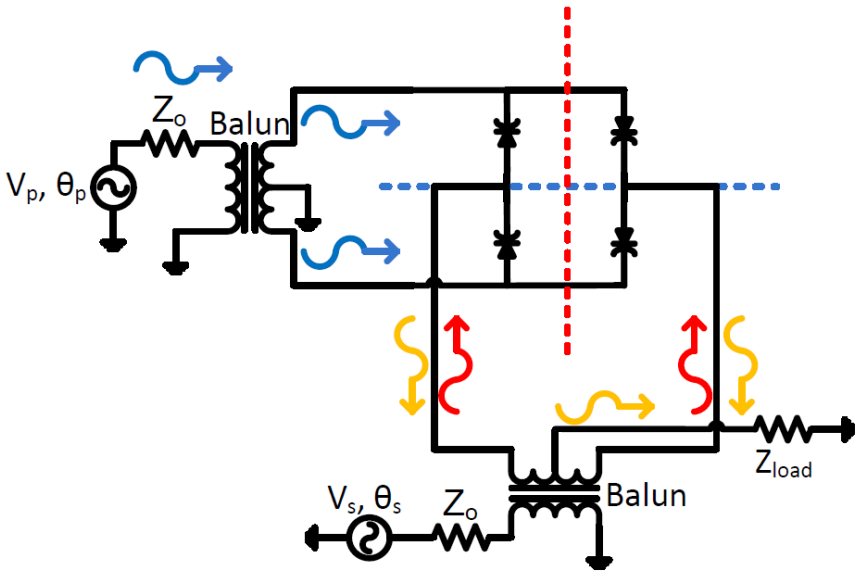

Figure 4.18: A double-balanced mixer showing the incident and reflected source, pump, and output waves. By Conservation of Phase, the reflected source waveforms will be in-phase and will combine at the center tap of the secondary of the source balun.

The double-balanced mixer provides balanced differential signals at both the pump and

source frequencies to each of the four ring diodes. Assuming ideal baluns, the incident balanced pump waveforms (blue) and source waveforms (red) will be of equal amplitude and perfectly 180 degrees out of phase. The differential action of the baluns force a virtual ground for both the incident pump waveforms (blue dashed line) and source waveforms (red dashed line) at the varactor diode terminals. Connecting the pump circuit to the source circuit's virtual ground and vice versa provides broadband isolation between the two. The incident source waveforms interact with the pumped varactors in anti-phase such that by the Conservation of Phase for mixers the reflected waveforms must be in-phase. The source reflected waves then combine to the center tap of the secondary of the source balun to form the output.

To better understand how the Conservation of Phase for mixers guarantees the source reflected waves will be in-phase with each other, consider the equivalent source circuit in Fig. 22. In each branch, the varactors are connected in anti-parallel but the polarity of the pumping voltage ensures that the change in capacitance is identical. Because of the differential pumping of the varactors, the pump voltage phase relationship between branch 1 and branch 2 will always be 180 degrees. Therefore, regardless of the dot convention of either the source or pump balun the possible phase of each reflected source waveform is

$$Branch1: \phi_p - \phi_s = 0^\circ or 180^\circ - 0^\circ = 0^\circ or 180^\circ \tag{4.128}$$

$$Branch2: \phi_p - \phi_s = 180^\circ or 0^\circ - 180^\circ = 0^\circ or -180^\circ \tag{4.129}$$

such that the reflected source wave in branch 1 will always be in phase with the reflected source wave in branch 2.

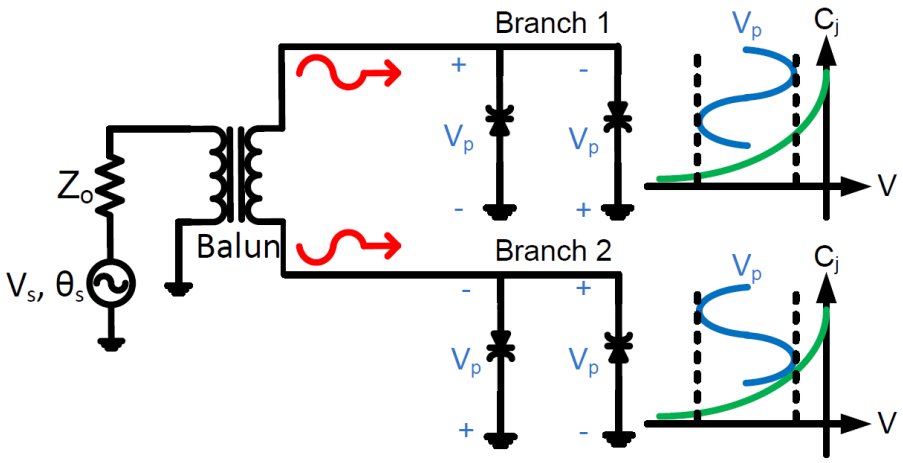

Figure 4.19: Equivalent circuit from the perspective of the source generator. The polarity of the pumping voltage across each varactor is indicated to illustrate how Conservation of Phase for mixers will guarantee the reflected waves will always be in-phase.

Fig. 4.20 shows the circuit design of the phase-coherent degenerate parametric amplifier in the DBM architecture. Varactor diodes were selected to act as the nonlinear capacitive mechanism. The design in Fig. 4.20 was implemented in a single-tone harmonic

balance simulator with the source frequency set as the fundamental (note that the source and pump frequencies are commensurate in a degenerate paramp, so only one fundamental is needed), using standard SPICE models for all components. The varactor diodes are the BB857 model that have an available junction capacitance range of approximately 0.5 pF at their maximum reverse bias voltage of 30 V to 6.6 pF at zero volt bias. Each varactor was doubled-up in parallel to center the capacitance-voltage curve for maximum gain. Surface-mount transforming baluns were chosen (Minicircuits TC4-25+), and RF crossovers were needed for routing traces in a single-layer microstrip environment. The prototype circuit was fabricated on 62 mils thick Rogers 4350 RF substrate material with 1 oz copper plating, as seen in Fig. 24.

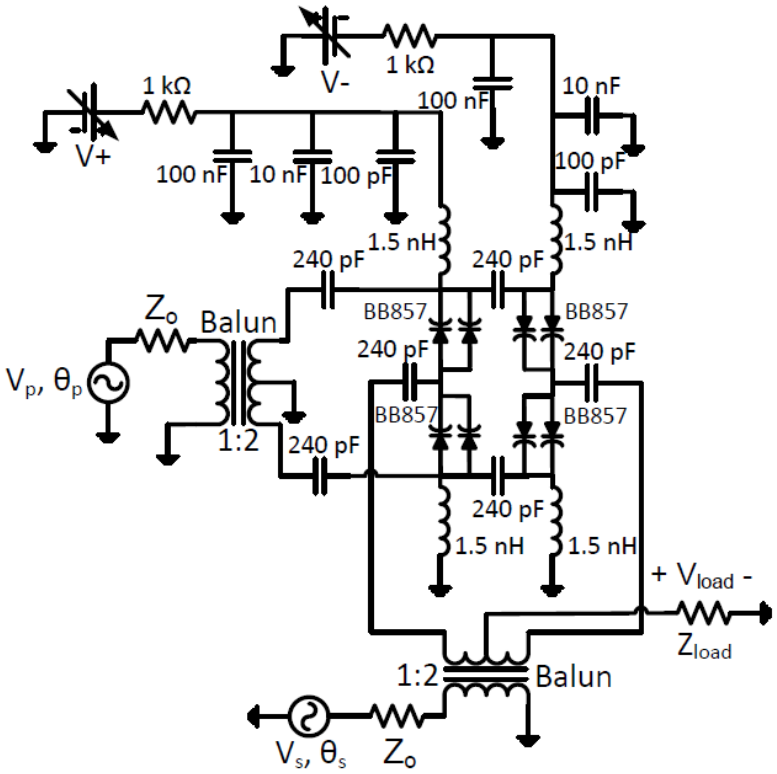

Figure 4.20: Circuit schematic of the double-balanced phase-coherent degenerate parametric amplifier showing all component values.

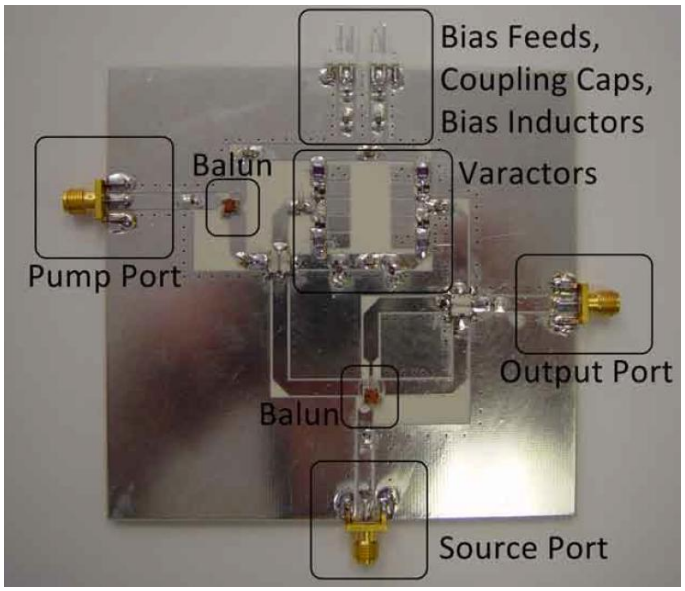

Figure 4.21: Photograph of the prototype double-balanced phase-coherent degenerate parametric amplifier board with critical components identified and labeled.

To test the prototype, a test bench setup was constructed. This setup used two phase-locked RF signal generators (one of which has the capability of phase adjustment) to produce the phase-coherent single-tone pump and source signals, as seen in Fig. 4.22. The output of the degenerate parametric amplifier was monitored by a spectrum analyzer to confirm stable operation.

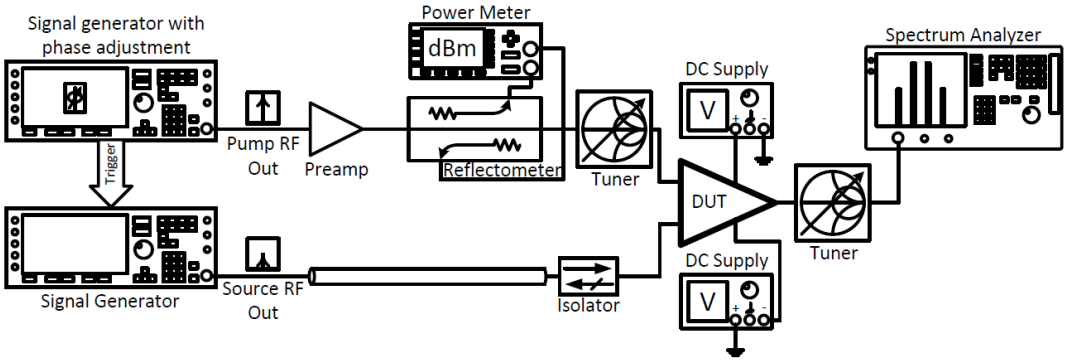

Figure 4.22: Test bench setup to measure gain, bandwidth, and stability of the phase-coherent degenerate parametric amplifier.

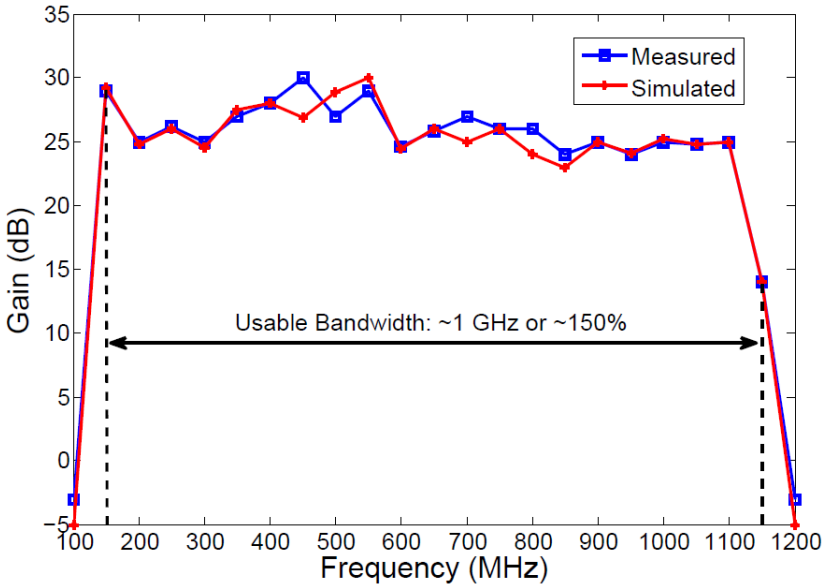

Figure 4.23: Plot of the simulated and measured gain versus source frequency of the double-balanced phase-coherent degenerate paramp at a constant pump power level of 30 dBm.

Fig. 26 compares the simulated and measured gain versus source frequency of the double-balanced phase-coherent degenerate parametric amplifier at a constant pump power level of 30 dBm. This large of a pump power level was required to maximize the capacitance switch of the varactors. If lower breakdown voltage varactors had been available with similar capacitance-voltage characteristics, the necessary pump power level might have been considerably less.

Ripple can be seen in both the simulated and measured gain plots within their usable bandwidths. As the source frequency varies, phase coherence is not perfectly maintained and the amplitude of the voltage waveform at ω_p across each varactor diode fluctuates. These two factors contribute to a slight change in the negative resistance value that causes the gain ripple. In addition, the gain drops below zero when 150 MHz $> f_s >$ 1150 MHz as it exceeds the operational bandwidth of the baluns. The average gain within the usable bandwidth of the amplifier is approximately 26 dB.

c) Phase-Coherent Upconverting Parametric Amplifiers

The analysis above demonstrated that an architecture similar to that of a phase-coherent degenerate parametric amplifier could be used to demonstrate a phase-coherent upconverting amplifier. The degenerate parametric amplifier prototype developed in the above section does not use any output filtering and was intended to operate under the condition $\omega_p = 2\omega_s$ making it ideal to demonstrate phase-coherent upconversion.

Figure 27 compares the simulated and measured transducer gain versus the upconverted output frequency in addition to predicted values according to the analytical model in (3.66). Ripple in the gain can be seen within the usable bandwidth. Inspection of (3.66) shows that term 1 in the denominator is sensitive to changes in the source frequency and the

transformed source, pump, and load conductances. Small perturbations in these values causes large changes in the transducer gain resulting in gain variations across the usable bandwidth. In addition, the gain drops below a usable value when 1.5 GHz $> 3f_s >$ 2.1 GHz. This is a result of bandwidth limitations of the source and pump baluns that introduce losses that cannot be overcome by the negative resistance.

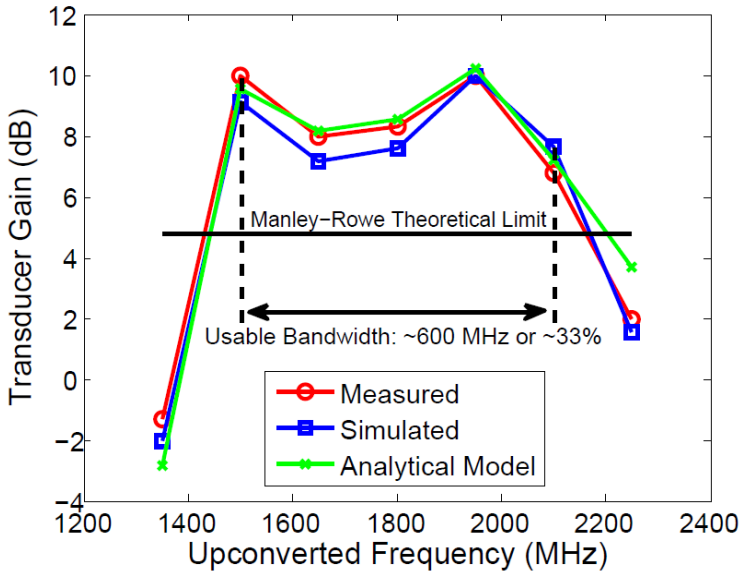

Figure 4.24: Simulated and measured transducer gain versus upconverted output frequency in addition to predicted values according to the analytical model in (3.66).

Figure 4.24 also shows the theoretical phase-incoherent upconverting parametric power power gain limit imposed by the Manley-Rowe relations. As predicted, the Manley-Rowe relations are incapable of predicting upconverted gain when the source and pump frequencies are phase-coherent. In addition, the achievable gain goes beyond what the Manley-Rowe relations would state is the theoretical limit for parametric upconversion.

G) Stability Analysis of Parametric Amplifiers

The strong nonlinearity of the nonlinear reactance in parametric amplifiers gives rise to situations when they can sustain an oscillation at a frequency different from those delivered by the source and pump generators or their harmonic combinations. As a result, paramps can be classified as autonomous microwave circuits. Stability analysis of autonomous microwave circuits is difficult due to their inherent nonlinearity and the usual coexistence of the oscillatory solution with a mathematical solution for which the circuit does not oscillate. Traditionally, two-port amplifier stability is determined by investigating the small-signal regime of the circuit and determining if for some frequency interval $(\omega_{min}, \omega_{max})$ the S-parameters of the amplifier satisfy the Rollet stability criteria. While parametric amplifiers are inherently three-port networks, they can be reduced to a two-port by linearizing the circuit equations about either the large-signal pump periodic regime (for large-signal stability analysis) or the small-signal

source regime (for small-signal stability analysis). Typically, though, the Rollet stability criteria is not applicable to parametric amplifiers as it assumes the circuit is intrinsically stable and is a single-frequency device. However, the combination of the Manley-Rowe relations and the analytical models developed above provide a simplified set of tools to analyze the stability of parametric amplifiers under various perturbations, operating conditions, and input and output reflection coefficients, Γ_{in} and Γ_{out}, respectively.

a) Conditional Stability of Phase-Incoherent Upconverting Parametric Amplifiers

While the Rollet stability criteria is limited to single-frequency two-port amplifiers (and thus not applicable to parametric upconverters), the general concepts of the theory can still provide a means to begin a stability analysis of phase-incoherent upconverting parametric amplifiers. By the Rollet stability criteria, a two-port amplifier is said to be unconditionally stable in the small-signal regime if $\Re\{Z_{in}(\omega)\} > 0$ for any passive complex load Z_L and $\Re\{Z_{out}(\omega)\} > 0$ for any passive complex source Z_s within the entire frequency interval $(\omega_{min}, \omega_{max})$. From the perspective of the source generator, any standing wave would be at ω_s, and from the perspective of the output, any standing wave would be at $\omega_o = \omega_s + \omega_p$. Therefore, the condition of the real part of the input and output impedances remaining positive should be satisfactory to determine upconverting parametric amplifier stability in the small-signal regime with the caveat that Z_{in} and Z_{out} be analyzed independently. Figure 28 shows a phase-incoherent upconverting parametric amplifier whose nonlinear reactance, circuit isolation filters, and pumping circuit have been placed inside a ``black box.'' The amplifier is being driven by an AC generator at frequency ω_s with a Thévenin impedance Z_s. The output circuit of the parametric amplifier has been terminated in an impedance Z_L resulting in a reflection coefficient Γ_L.

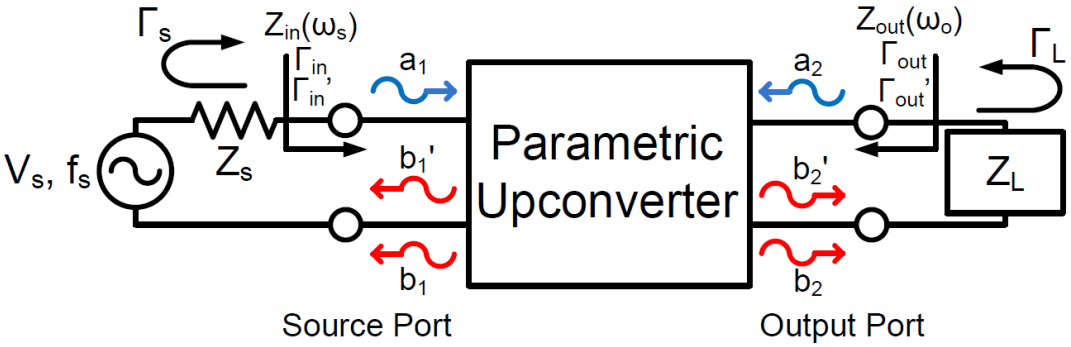

Figure 28: A black box phase-incoherent upconverting parametric amplifier. The incident and reflected source and output waves can be expressed independently of one another, allowing for the two ports to be analyzed individually.

Unconditional stability in the small-signal regime is guaranteed if the magnitude of the total reflection coefficients seen at the source and output ports are less than or equal to 1

within the frequency interval $(\omega_{min}, \omega_{max})$ since this implies the real parts of the complex impedances $Z_{in}(\omega_s)$ and $Z_{out}(\omega_o)$ are non-negative. S-parameter analysis of the circuit in Fig. 28 can only be achieved if the circuit is treated as a one-port from, first, the perspective of the source, and, second, from the perspective of the output. Let

$$\Gamma_{in} = \frac{b_1}{a_1} \tag{4.130}$$

be the input reflection coefficient without considering a substantial reverse-transfer wave $b_1^{'}$. In other words, Γ_{in} is only a measure of impedance mismatch between the source generator and the phase-incoherent upconverting parametric amplifier's source port. Then, let

$$\Gamma_{in}^{'} = \frac{b_1 + b_1^{'}}{a_1} \tag{4.131}$$

be the total input reflection coefficient when considering the superposition of b_1 and $b_1^{'}$. By S-parameter network theory,

$$a_2 = \Gamma_L b_2 \tag{4.132}$$

$$b_2 = (1 - \Gamma_{in}) S_{21} a_1 \tag{4.133}$$

$$b_1^{'} = S_{12} a_2 . \tag{4.134}$$

Substitution of (4.3), (4.4), and (4.5) into (4.2) yields

$$\Gamma_{in}^{'} = \Gamma_{in} + S_{12} S_{21} \Gamma_L (1 - \Gamma_{in}). \tag{4.135}$$

From the Manley-Rowe relations, the idealized power gain of a phase-incoherent upconverting parametric amplifier can be expressed as $\frac{\omega_o}{\omega_s}$. Above it was noted that a parametric downconverter will always attenuate with an idealized minimum loss of $\frac{\omega_o}{\omega_s}$, where, for the downconverter, the down-converted output frequency ω_o is always less than the source input frequency ω_s. In addition, by the Conservation of Phase for mixers, the output of a parametric upconverter must have a relative phase equal to the sum of the relative phase of the source and the relative phase of the pump, ϕ_s and ϕ_p, respectively, and, similarly, the relative phase of the output from a parametric downconverter must be the difference between the source and pump relative phases. Finally, the forward and reverse power gain is related to S-parameter network theory by the square of S_{21} and S_{12}. Therefore, for a phase-incoherent upconverting parametric amplifier the forward- and reverse-transfer coefficients can be expressed as

$$S_{21} = \sqrt{\frac{\omega_o}{\omega_s}} \angle \phi_p \tag{4.136}$$

$$S_{12} = \sqrt{\frac{\omega_s}{\omega_o}} \angle -\phi_p. \tag{4.137}$$

It is important to note that the Manley-Rowe relations are independent of the shape of the nonlinearity curve of the nonlinear reactance, the manner in which harmonic currents are isolated, and how each harmonic current is terminated. As a result, the definition of S_{21} and S_{12} in (4.136) and (4.137) do not change for any passive reflection coefficient Γ_s or Γ_L. Equation (4.6) can now be simplified to

$$\Gamma_{in}^{'} = \Gamma_{in} + \left(\sqrt{\frac{\omega_s}{\omega_o}} \angle \phi_p \right) \left(\sqrt{\frac{\omega_o}{\omega_s}} \angle -\phi_p \right) \Gamma_L \left(1 - \Gamma_{in}\right) = \Gamma_{in} + \Gamma_L \left(1 - \Gamma_{in}\right) \leq 1, \tag{4.138}$$

which is guaranteed to be less than or equal to 1 for any source frequency ω_s at any source power drive level that does not approach that of the pump and passive reflection coefficients Γ_s and Γ_L. Performing a similar derivation for the output port, it can be shown that

$$\Gamma_{out}^{'} = \Gamma_{out} + S_{21} S_{12} \Gamma_s \left(1 - \Gamma_{out}\right) \leq 1, \tag{4.139}$$

where

$$\Gamma_{out}^{'} = \frac{b_2 + b_2^{'}}{a_2} \tag{4.140}$$

$$\Gamma_{out} = \frac{b_2}{a_2}, \tag{4.141}$$

and S_{21} and S_{12} are defined by (4.139) and (4.140). Equation (4.141) is guaranteed to be less than or equal to 1 for any output frequency ω_o at any source power drive level that does not approach that of the pump and passive reflection coefficients Γ_s and Γ_L.

From the analysis presented above, it would appear that phase-incoherent upconverting parametric amplifiers are unconditionally stable for any and all frequencies and input drive levels. However, this analysis focused on the small-signal response of the amplifier in the small-signal regime by linearizing its response to the large-signal pumping source. To complete the stability analysis of upconverting parametric amplifiers, the circuit must be linearized about the large-signal pumping source to determine its response in the periodic large-signal regime.

An analysis performed demonstrated the capability of oscillation for a nonlinear

capacitance being pumped by a periodic large-signal source. It was assumed that the circuit was lossy and contained some inductive reactance. At some pumping power threshold the circuit will exhibit a flip bifurcation resulting in a steady-state subharmonic oscillation at the natural frequency $\omega_o = \frac{\omega_p}{2}$. The former periodic solution occurring at ω_p continues to exist after the flip bifurcation, but it has become unstable. Beyond the threshold point the only observable solution is the frequency-divided solution.

Combining the small-signal and large-signal analysis for phase-incoherent upconverting parametric amplifiers it can be seen that they are conditionally stable. It should be noted that the possibility of a flip bifurcation was not explored in the small-signal analysis as it was assumed that the amplifier was intrinsically stable when linearized about the small-signal solution and that the input source drive level would never approach that of the pumping source. To do so would lead the analysis out of the small-signal regime and into the large-signal regime.

b) Conditional Stability of Negative-Resistance Parametric Amplifiers

The analytical models developed above regarding both degenerate and non-degenerate parametric amplifiers shows the generation of a negative resistance. Power gain is possible when the negative resistance is large enough as the circuit attempts to balance the excess negative resistance exhibited by the nonlinear reactance with the positive resistance presented by the losses of the surrounding linear circuitry. However, when the value of the negative resistance exceeds the positive losses of the circuit, balance cannot be maintained, and the circuit will become unstable. From (3.46), large-signal stability will be maintained for degenerate parametric amplifiers when

$$G_s + \frac{(\omega_s b)^2}{2G_L G_p} P_L > \frac{\omega_s b I_p}{2G_p}. \tag{4.142}$$

To better understand the conditions for large-signal stability, assume that the source conductance G_s is small compared to $\frac{(\omega_s b)^2}{2G_L G_p} P_L$. Then, (4.142) reduces to

$$I_p < \frac{\omega_s b P_L}{G_L}. \tag{4.143}$$

Let $P_L = V_s^2 G_L$ such that

$$I_p < \omega_s b V_s^2 = \omega_s C_{s,NL} V_s, \tag{4.144}$$

where $C_{s,NL}$ is a measure of the nonlinearity of the capacitance-voltage curve of the nonlinear

reactance. It is now useful to define a new positive resistance, $R_{stab} = \frac{V_s}{I_p}$, that relates the peak value of the voltage waveform across the nonlinear reactance at the source frequency to the peak value of the pump current generator such that

$$R_{stab} > \frac{1}{\omega_s C_{s,NL}}. \tag{4.145}$$

Evaluating the inequality of (4.145) shows that as the pump drive level is increased, R_{stab} decreases, and eventually will fall below the stability threshold resulting in unstable operation. In addition, an unexpected result comes from this inequality. Decreasing $C_{s,NL}$, and all else being unchanged, can eventually lead to instability. $C_{s,NL}$ is a measure of nonlinearity of the nonlinear reactance at the DC operating point. To decrease the nonlinearity when using, say, a varactor diode as a voltage-dependent nonlinear capacitor, one would increase the DC bias voltage such that the operating point sat in the linear portion of the capacitance-voltage curve. At first this would seem counterintuitive based on the large-signal transducer gain analytical model. However, (4.145) seems to suggest that a decrease in the nonlinearity of the nonlinear reactance at the DC operating point has an overall effect of increasing the negative resistance seen by the source resulting in an increase in the power gain. Following a similar derivation for non-degenerate parametric amplifiers, and using the transducer gain analytical model in (4.48), the criteria for stable operation can be shown to be

$$R_{stab} > \frac{1}{\sqrt{\omega_i \omega_s} C_{s,NL}}. \tag{4.146}$$

A phase-coherent degenerate parametric amplifier was designed based on the analytical models developed above. Because of the direct relationship between gain and stability in the large-signal regime, and the sensitivity of stability to small perturbations, an in-depth stability analysis of phase-coherent negative-resistance parametric amplifiers is warranted.

As discussed, to obtain the maximum gain in phase-coherent degenerate parametric amplifiers, the phase condition $\phi_p = 2\phi_s$ must be imposed. The pump power must also be properly selected, which is generally done through a power sweep, most often using a commercially-available harmonic balance (HB) simulator. Inspection of (4.16) shows that perturbations in the pump power level results in changes in R_{stab} that could potentially destabilize the amplifier. Therefore, to continue the stability analysis of phase-coherent degenerate parametric amplifiers the evolution of the system poles will be determined under variations in the pump power level.

The poles are obtained by, first, inserting a small-signal current source of value I_s at a perturbation frequency, Ω, in parallel with a sensitive circuit node such as the cathode of a varactor diode. Next, the conversion-matrix approach is applied to linearize the circuit about each particular steady-state solution. A closed-loop transfer function, Z(Ω), can then be

defined as the ratio between the node voltage and the perturbation current I_s. Finally, the fitting of Z(Ω) with a quotient of polynomials numerically provides the poles associated with each steady-state solution. Figure 29 shows the evolution of the system poles of the phase-coherent degenerate parametric amplifier developed above at f_s = 400, 650, and 900 MHz as the pump power level is swept from 28 dBm to 35 dBm. It can be seen that a set of complex poles at 650 MHz cross the imaginary axis into the right-half plane approximately when P_p = 30.85 dBm, resulting in a flip bifurcation. However, the amplifier appears to be stable within its usable bandwidth below P_p = 30.5 dBm.

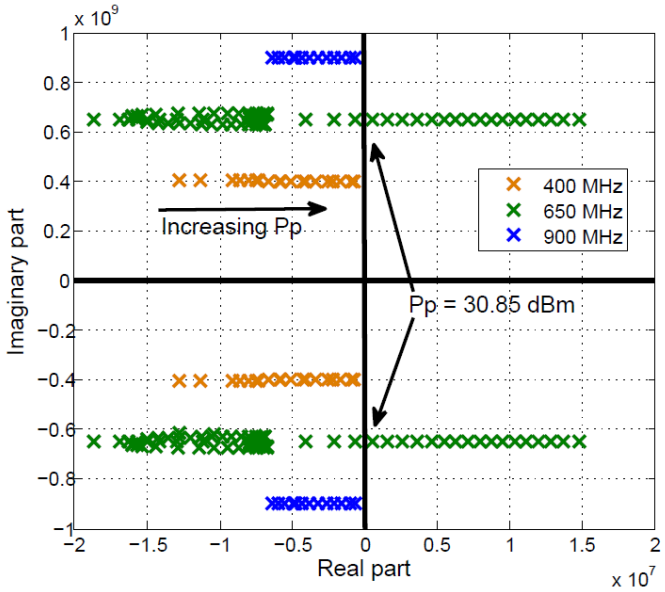

Figure 4.25: Evolution of the system poles of the phase-coherent degenerate parametric amplifier as the pump power level is swept. A set of complex poles at 650 MHz cross the imaginary axis at about P_p = 30.85 dBm causing a flip bifurcation and destabilizing the amplifier. The paramp appears to be stable when $P_p <$ 30.5 dBm.

With phase-coherent degenerate parametric amplifiers, a flip bifurcation results in the coexistence of an oscillatory solution at the same frequency as the source input. The evolution of the system poles in Fig. 29 provides no insight into the implications of this instability on the solution curves in the periodic regime as this is dependent on the initial conditions of the amplifier and the relative phase of the oscillatory solution with respect to the source input.

The stability properties of periodic regimes are determined by the Floquet multipliers with the number of multipliers agreeing with the system dimension N. In the frequency domain, stability is analyzed in terms of the poles, or roots, of the characteristic determinant of the harmonic balance (HB) system perturbed about the periodic regime. This determinant can be written in a compact manner as $det\left[JH\left(k\omega_s + p\right)\right] = 0$, where J is the Jacobian matrix and k = -NH to NH, where NH is the number of harmonic terms. There is a non-univocal relationship

between the poles and the multipliers, given by $m_i = e^{p_k^i T}$, with i = 1 to N and T_s the solution period. Thus, there is a set of poles $p_i^k = p_i^0 + jk2pi$, with k an integer and p_i^0 a ``canonical'' pole associated with multiplier m_i. The critical poles, $p = \pm j\omega_s = \pm j\frac{\omega_p}{2}$, are associated with the multiplier $m_1 = e^{\pm j\frac{\omega_p}{2}T_s} = 1$. Also associated with m_1 is a pole with value zero, $p = 0$. For $p = 0$, the characteristic determinant agrees with the determinant of the Jacobian matrix of the original HB system. Therefore, the HB system should become singular at the bifurcation point with the critical poles $p = \pm j\frac{\omega_p}{2}$. This singularity can give rise to a turning point of the solution curve or to the onset of new solution paths at the same fundamental frequency ω_s.

To illustrate this, it will be assumed that prior to the bifurcation (occurring at η_o) there is only one solution per parameter value (single curve). Let $\overline{X}_o$ be the HB solution at the bifurcation $\overline{H}\left(\overline{X}, \eta_o\right) = 0$. For an arbitrarily small increment $\Delta\eta$, the HB system can be linearized about $\overline{X}_o$. Then it is straightforward to demonstrate that the generation of new solution branches from $\overline{X}_o$ is only possible in the case of a singular Jacobian matrix $\frac{\partial\overline{H}}{\partial\overline{X}_o}$. This situation can be associated with a pitchfork bifurcation ruled by the transformation

$$S_o \rightarrow 2S_o^{'} + S_1, \tag{4.147}$$

where the sub-index indicates the number of unstable poles. At the bifurcation, the original solution curve S_o becomes unstable (S_1) and gives rise to two distinct stable solutions $S_o^{'}$. In fact, this pitchfork bifurcation is difficult to observe in practice because it requires particular symmetry conditions. Instead, the system exhibits an imperfect pitchfork bifurcation.

Utilizing the simulations and prototype board, solution curves were obtained across multiple frequency and operating points. At f_s = 716 MHz, the output-power curve obtained with a HB simulation passes through a maximum, then begins to decrease, as seen in Fig. 4.26. The evolution of the system poles in Fig. 29 shows that at the sharp maximum near 650 MHz a pair of complex conjugate poles, $\sigma \pm j\frac{\omega_p}{2}$, cross the imaginary axis into the right half of the complex plane. However, there is no clue on how the system evolves after this bifurcation point. In fact, the remainder of the curve obtained in HB is unstable and unobservable.

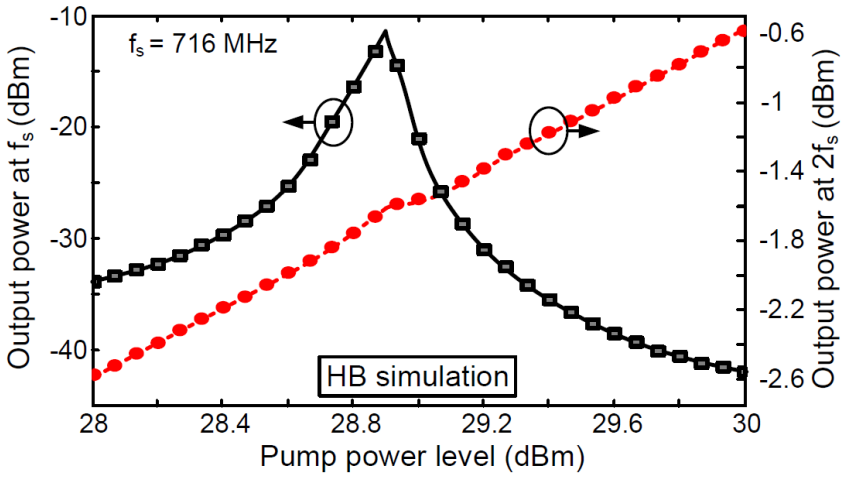

Figure 4.26: Solution curve of the phase-coherent degenerate parametric amplifier at f_s = 716 MHz using a HB simulation.

To search for other possible solution paths, auxiliary generators (AGs) were connected in parallel between the terminals of one of the varactor diodes. The AG operates at the source frequency, $\omega_{AG} = \omega_s$, and allows implementation of a parameter-switching technique. To obtain high slope sections of the solution curves, the AG amplitude, V_{AG}, is swept, optimizing both the AG phase, ϕ_{AG}, and the pump power in order to fulfill the non-perturbation condition $Y_{AG} = \frac{I_{AG}}{V_{AG}} = 0$, where I_{AG} is the current passing through the AG, V_{AG} is the voltage across the terminals of the AG, and Y_{AG} is the admittance seen by the AG. Using this technique, it was possible to complete the solution curves seen in Figs. 4.27(a) and (b).

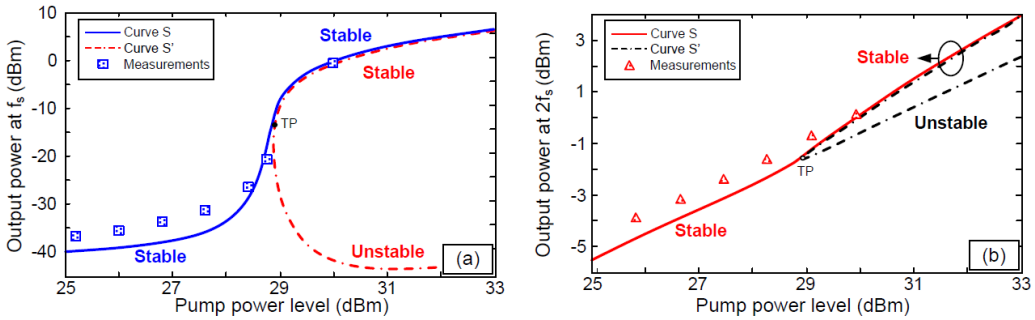

Figure 4.27: Analysis of the branching phenomenon of the phase-coherent degenerate parametric amplifier at f_s = 716 MHz.

The original curve, S, in Fig. 31(a) is continuous and quickly grows to high output power values at ω_s. There is a second path that only exists on the right hand side of Fig. 31(a), from the turning point TP (Pp=28.9 dBm). The upper section of this second path (S') is very

close to the high power section of the original curve (S). Note that the HB simulation evolves from curve S to curve S' instead of following the fast power increase of the original curve S . In the higher output power section, the two curves S and S' have very similar amplitude values, however, they have a phase shift close to 180° at ω_s . To confirm that the difference is not due to an analysis inaccuracy, the solutions obtained with the AG have been introduced as initial conditions in the HB simulation and produced identical results.

Unlike the transformation in (4.18), there is no branching point in the curves in Fig. 31. In spite of this, the geometry of the paths suggest the possible occurrence of an imperfect pitchfork bifurcation. In this bifurcation, the original solution path (assumed stable here) S_o exists for the whole parameter interval and maintains its stability properties. However, a new independent path, with a turning point, is generated close to the original one. When the parameter is varied from the original regime S_o towards the bifurcation, the transformation at the bifurcation point is

$$S_o, \phi \rightarrow S_o' + S_1', \tag{4.148}$$

where the second relationship indicates that there are no solutions (ϕ) in path S' before the bifurcation, and two solutions, one stable and the other unstable, after this bifurcation. Note that there is one solution prior to the bifurcation and three solutions after this bifurcation for both the perfect and imperfect pitchfork bifurcations.

To verify the above assumptions, pole-zero identification has been applied along the two solution paths in Fig. 31 with the results in Fig. 32. Curve S is stable for all values of P_p . Its dominant poles, $\sigma \pm j\frac{\omega_p}{2}$, approach the imaginary axis near the high slope section but do not cross this axis. In the case of the path S', a pair of complex-conjugate poles $\sigma \pm j\frac{\omega_p}{2}$ cross the imaginary axis at P_p = 28.9 dBm; the upper section is stable and the lower section is unstable. The stability analysis confirms the existence of a transformation of the form in (4.19). This stability study explains the differences between simulations and measurements encountered in the pole-zero analysis in Fig. 4.28.

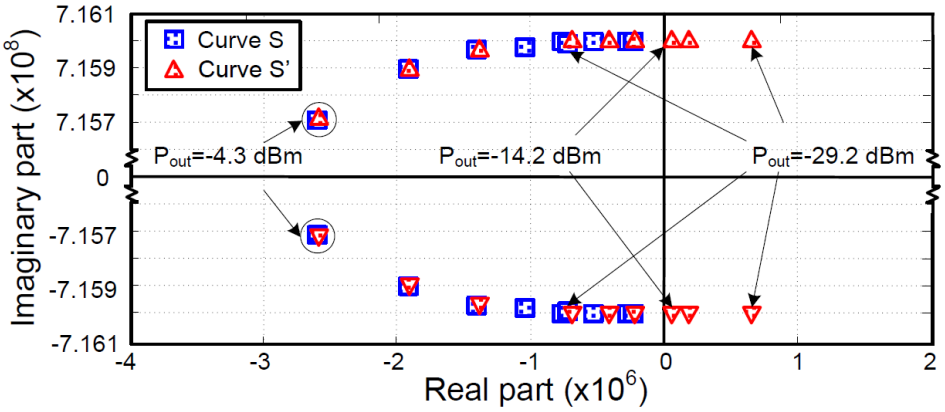

Figure 4.28: Stability analysis using pole-zero identification of the solution curves.

According to the above analysis there are two stable solutions with very similar output power values coexisting for pump power values larger than 28.9 dBm. The existence of two stable solutions can be related to the fact that the instability gives rise to a frequency division-by-2 of the pump signal. In standard divide-by-2 frequency dividers (without an independent source at the divided-by-2 frequency), two identical solutions with 180° phase shifts coexist after the bifurcation. In fact, the two solutions in the upper section of Fig. 31(a) have a phase difference close, but not identical to, 180°. The small difference in magnitude is attributed to the presence of an independent source at $\omega_s = \frac{\omega_p}{2}$. The power difference increases with increasing source power level, as seen in the simulation of Fig. 4.29. In fact, the physical observation of one solution or another will depend on the initial conditions of the amplifier.

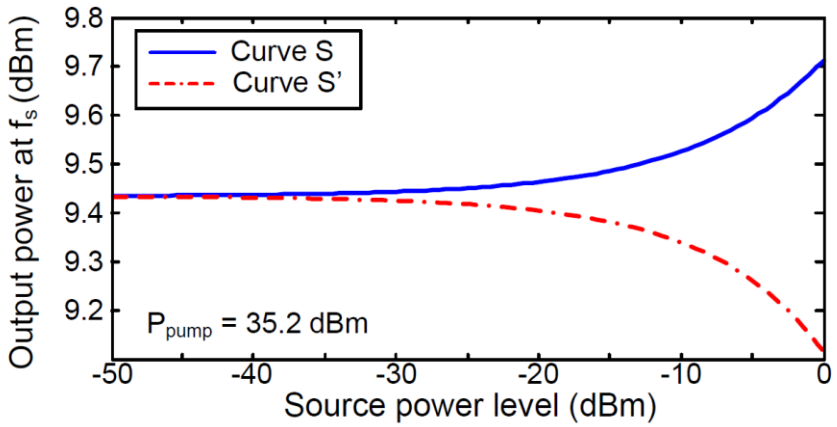

Figure 4.29: Variation in the output power at f_s versus increasing source power level showing two possible solution curves that are dependent on the initial conditions of the phase-coherent degenerate parametric amplifier.

For f_s = 650 MHz, there is a qualitative change in the circuit behavior, as seen in Fig.

4.30. Curve S exhibits the turning point (TP2) whereas curve S' does not change its stability properties in the neighborhood of this point. Curve S (providing the only circuit solution for small pump power levels) becomes unstable at TP2, so the system necessarily jumps to the upper curve section in agreement with the measurement results.

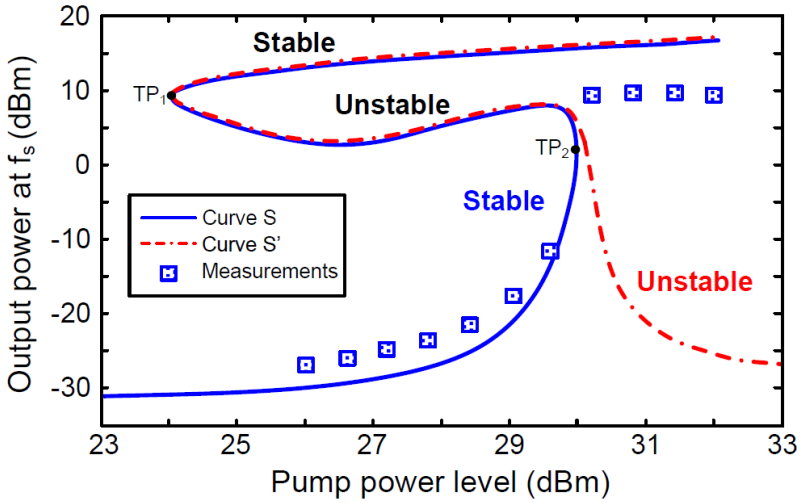

Figure 4.30: Solution curve for the phase-coherent negative-resistance degenerate parametric amplifier at f_s = 650 MHz.

7. Summary and Conclusions

The purpose of this seedling research project was to investigate the feasibility of using multiferroic materials for advanced RF applications. The project was divided into three parallel tasks of materials growth, device design, and circuit design. The materials growth effort was specifically aimed at epitaxial quality Terfenol-D, an alloy of Terbium, Dysprosium, and Iron ($Tb_xDy_{1-x}Fe_{2-y}$) that exhibits large magnetostriction at room temperature and relatively small applied magnetic fields. The use of a piezoelectric substrate was proposed to provide the mechanical coupling necessary to achieve electric-field tunable materials. An initial approach using one MBE chamber was explored. However, mechanical issues prevented this approach from yielding any usable materials. A secondary approach was attempted using separate MBE chambers and vacuum-locked wafer transport. Some results were obtained using this technique. However, oxidation of the metal layers, particularly Tb, prevented any successful alloyed-layer growth of Terfenol-D.

The device design task consisted of electromagnetic simulation of transmission line structures, specifically coplanar waveguide (CPW), using Terfenol-D layers on Lithium Niobate ($LiNbO_3$) substrates. Simulations of phase velocity change were conducted to assess the extent to which the magnetic properties (permeability) of Terfenol-D would change the phase velocity. Of course, the phase velocity change was also due to the change in permittivity of the piezoelectric substrate. Simulations indicated approximately a 1.4:1 change in phase velocity could result from the shifts in permittivity and permeability due to an applied bias voltage. Such phase velocity changes could result in usuable devices for various tunable RF applications.

The circuit design aspect of this project consisted entirely of a study of parametric amplifiers (paramps). Such amplifiers result from a change in reactive impedance (*i.e.* associated with a phase velocity change) due to applied RF voltages. In this manner, high-efficieciency, and potentially wideband RF power amplifiers could be achieved. Because this task was executed in parallel with the materials growth and device design, no circuit designs using multiferroic materials was possible. Instead, conventional semiconductor varactor devices were used to assess the feasibility of RF power paramps. Extensive circuit modelling was performed, and prototype circuits were constructed. Some successes were achieved in the development of wideband amplifiers based on double-balanced mixer circuit topologies. In addition, efficiencies approaching 50% were achieve for narrow band parametric amplifiers.

In conclusion, it is clear that significantly more research must be performed on multiferroic materials growth in order to achieve any successes at the device or circuit level. If sufficient improvement in materials quality is obtained, the device and circuit simulations and prototypes indicate some feasibility of the approach of using multiferroic materials for advanced RF applications.

6. References

1) B. Gray, J. S. Kenney, and R. Melville, “Analytical Modeling of Microwave Parametric Upconverters,” in *IEEE Trans. Microwave Theory and Tech.*., Vol. 58 No. 8 pp. 2118-24, Aug. 2010.
2) B. Gray, F. Ramirez, R. Melville, A. Suarez, and J. S. Kenney, “A Broadband Phase-Coherent Degenerate Double Balanced Parametric Amplifier,” in *IEEE Microwave and Wireless Comp. Lett.* Vol. 21, No. 11, pp. 607-09, Oct. 2011.
3) B. Gray, R. E. Melville, and J. S. Kenney, “Behavioral Modeling and Simulation of a Parametric Power Amplifier,” in *2009 IEEE MTT-S Int. Microwave Sym. Dig.* June 7-12, 2009, Boston, MA, pp. 1373-76.
4) M. Masood, B. Gray, R. Melville, M. Omer, and J.S. Kenney, “Modeling and Linearization of a Parametric Power Amplifier,” in Proc. 40th European Microwave Conference, Sep. 26-30, 2010, Paris, France.
5) B. Gray, M. Pontón, A. Suárez, J. S. Kenney, “Analytical Modeling of Transducer Gain and Gain Compression in Degenerate Parametric Amplifiers,” in 2012 IEEE Radio and Wireless Symp. Dig., Jan. 15-18, 2012, Santa Clara, CA.